Available online at www.sciencedirect.com

SciVerse ScienceDirect

Geochimica et Cosmochimica Acta 76 (2012) 103–124

Geochimica et Cosmochimica Acta

www.elsevier.com/locate/gca

Agglomeratic olivine (AO) objects and Type II chondrules in ordinary chondrites: Accretion and melting of dust to form ferroan chondrules

Alex Ruzicka [a,*], Christine Floss [b], Melinda Hutson [a]

[a] *Cascadia Meteorite Laboratory, Portland State University, Department of Geology, 17 Cramer Hall, 1721 SW Broadway, Portland, OR 97207-0751, USA*

[b] *Laboratory for Space Sciences and Physics Department, Washington University, Campus Box 1105, St. Louis, MO 63130, USA*

Received 20 January 2011; accepted in revised form 3 October 2011; available online 17 October 2011

Abstract

Agglomeratic olivine objects (AO objects) and possibly related chondrules in three ordinary chondrites (NWA 4910 [LL3.1], NWA 3127 [LL3.1], Sahara 98175 [LL3.5]) were studied using petrographic and microanalytical techniques to evaluate the origins of these materials. AO objects are mixtures of fine-grained ($\leqslant$5–10 μm-diameter) ferroan ($Fa_{12–35}$) olivine, troilite that is often concentrated towards the periphery of objects, pyroxene, feldspathic material, relict magnesian olivine and pyroxene grains, and relict chondrules. One micro-CAI with a grossite core was also found. AO objects commonly rim chondrules. AO objects show transitional variations in texture and chemistry with Type II chondrules, ranging from AO objects that are finer grained and show no evidence of melting (AO-U objects), to weakly melted and more melted AO objects (AO-WM and AO-M objects, respectively), to fine-grained Type II chondrules (olivine grain size ~5–60 μm), to coarse-grained Type II chondrules (olivine grain size ~10–250 μm across); S contents and Na/Al values are typically higher in AO objects than in Type II chondrules. The properties of AO objects and Type II chondrules are interpreted to reflect progressive heating of dust of quasi-chondritic composition, accompanied by grain coarsening during melting, partial loss of the most volatile elements (chiefly S, also Na) during evaporative melting, and back-reaction with gas, to form troilite-rimmed AO objects. Data-model comparisons suggest that progressive heating of chondritic dust to form AO objects and Type II chondrules could have occurred in a dusty environment to yield a transient, oxidizing gas of high pressure (~10^{-3} bar), with gas derived from vaporized dust being much (>500–1000× or even up to 10^4–10^5×) more abundant than ambient solar composition gas. AO objects are protochondrules, but are themselves composed of chondrule debris of different types, suggesting that they represent one step of a chondrule recycling process that also included chondrule disaggregation and additional chemical processing. Our data appear to be compatible with the nebular shock wave model for chondrule formation.

1. INTRODUCTION

Ordinary chondrites contain olivine-rich inclusions that appear to have formed primarily as aggregates of fine-grained ferrous olivine together with xenocrystic grains and rare CAIs (Weisberg and Prinz, 1994, 1996). Such inclusions have a granular or 'protoporphyritic' texture (Hewins et al., 1997) and typically appear nearly opaque in petrographic thin sections using transmitted light, owing to fine grain size and high troilite content (Weisberg and Prinz, 1994, 1996). They can be 'dark zoned' with margins that are especially opaque in transmitted light, owing to a high concentration of peripheral sulfide (Dodd and Van Schmus, 1971). The inclusions have been termed agglomeratic chondrules (Van Schmus, 1969; Weisberg and Prinz, 1994, 1996; Connolly and Love, 1998), and they comprise ~5% of the chondrule population in ordinary chondrites

* Corresponding author. Tel.: +1 503 725 3372; fax: +1 503 725 3025.

E-mail address: ruzickaa@pdx.edu (A. Ruzicka).

0016-7037/$ - see front matter © 2011 Elsevier Ltd. All rights reserved.
doi:10.1016/j.gca.2011.10.020

(Weisberg and Prinz, 1994) or ~2% of ordinary chondrites overall (Weisberg and Prinz, 1996). Such inclusions might be suitable precursors to chondrules (Weisberg and Prinz, 1996; Hewins, 1997; Hewins et al., 1997).

These inclusions have sizes similar to typical chondrules but differ from them in being finer-grained and in displaying more evidence for accretion than melting (Van Schmus, 1969; Weisberg and Prinz, 1996; Hewins et al., 1997). We will show that similar material is also present as fine-grained rims of obvious accretionary origin around cores composed of typical chondrules. Thus, we refer to inclusions and rims containing these materials as agglomeratic olivine objects or simply 'AO objects'. Specifically, we define AO objects to be composed chiefly of fine-grained ($\leqslant$5–10 μm diameter) olivine ($Fa_{12–35}$), with textures suggestive of incipient melting, that may be present as chondrule-sized inclusions or as rims around chondrules.

The overall goals of this study are to evaluate: (1) the origin of AO objects; (2) the relationship of AO objects to typical ferromagnesian chondrules; and (3) implications for the origin of chondrules.

This study involved the use of optical light microscopy (OLM), scanning electron microscopy (SEM), electron microprobe analysis (EMPA), and secondary ion mass spectrometry (SIMS) to analyze AO objects and chondrules in three weakly metamorphosed LL ordinary chondrites (NWA 4910, NWA 3127, Sahara 98175). The three chondrites span a range of low-to-moderate subtypes, including LL3.1 for NWA 4910 (also known informally as 'Begaa'; Okazaki and Nakamura, 2005; Weisberg et al., 2009), LL3.1 for NWA 3127 (Russell et al., 2005), and LL3.5 for Sahara 98175 (Grossman, 1999). This provides an opportunity for distinguishing primary (nebular) and secondary (metamorphic) features. Chondrules in NWA 3127 and Sahara 98175 were previously studied for trace elements (Ruzicka et al., 2008). Ours is the first study to characterize the trace element compositions of AO objects. Preliminary results were presented in abstract form (Ruzicka et al., 2010; Ruzicka and Hutson, 2011).

2. SAMPLES AND METHODS

Table 1 provides data concerning the materials and objects that were studied. Electronic Annex AE-1 provides additional petrographic data. Objects of interest in the sections were identified and characterized at Portland State University (PSU), using a Leica DM2500 petrographic microscope, and backscattered electron (BSE) imaging using a JEOL JSM-35C SEM. Petrographic data were used to select areas for subsequent *in situ* chemical analyses. EMPA was used to analyze major- and minor-elements using a Cameca SX-100 electron microprobe at Oregon State University, via remote access from PSU, and trace elements were analyzed by SIMS using the modified Cameca ims-3f ion microprobe at Washington University, according to techniques described by Zinner and Crozaz (1986a). Both EMPA and SIMS analyses were obtained using 'narrow-beam' (1-μm-diameter EMPA, 15–20-μm-diameter SIMS) and 'broad-beam' (40–50-μm-diameter EMPA and SIMS) conditions. As many of the objects that we studied are fine-grained (with grain diameters typically $\leqslant$5–10 μm), broad-beam analyses provide estimates of local bulk compositions. Broad or 'defocused' beam EMPA data (DB-EMPA) for objects were obtained using a combination

Table 1
Characteristics of agglomeratic olivine (AO) objects, Type II chondrules, and ultra fine-grained matrix lumps in ordinary chondrites NWA 4910, NWA 3127, and Sahara 98175.

Type	Igneous texture?	Olivine grain diameter (μm)[b]	Feldspathic areas, diameter (μm)[b]	Bulk composition	Objects[a]
AO-U ['unmelted']	No	$\leqslant$5	Not apparent, to $\leqslant$1–3	Often S-enriched	Beg-3, Beg-4 outer rim, Beg-6 rim, Beg-16 outer rim, Beg-16A, Beg-17X rim, NWA-11 outer rim, NWA-11A rim, NWA-11C rim, Sah98-3 rim
AO-WM ['weakly melted']	Variable	$\leqslant$5	$\leqslant$1–3, to not apparent	Often S-enriched	Beg-1 rim, Beg-2, Beg-7, Beg-13 rim, Beg-14 rim, Beg-16 inner rim, NWA-11 inner rim, Sah98-3A rim, Sah98-4B rim, Sah98-12 core, Sah98-12 rim, Sah98-13 rim
AO-M ['melted']	Yes	$\leqslant$10	$\leqslant$2–12 (glass)	Often S-enriched	Beg-4 inner rim, Beg-8, Beg-10[c], Beg-16 inner rim, Beg-17, Sah98-3A core
Fine II	Yes	5–60	$\leqslant$2–15 (glass)	Depleted in S and Na	Beg-6 core, Beg-13 core[d], Beg-14 core, Beg-18A, NWA-11A core, NWA-21, Sah98-3 core, Sah98-4B core[e], Sah98-5
Coarse II	Yes	10–250	$\leqslant$12–50 (glass)	Depleted in S and Na	Beg-1 core, Beg-4 core, Beg-5, Beg-11 (coarse object), Beg-15, Beg-16 core, Beg-17X core, NWA-6, NWA-11 core, NWA-15 core, Sah98-13 core
Ultrafine matrix lumps	No	$\leqslant$1	Not obvious	Fractionated	Beg-12, Beg-17A

[a] Object designations: Beg = NWA 4910, also known informally as 'Begaa' (Okazaki and Nakamura, 2005) (PTS CML0379-A), NWA = NWA 3127 (PTS CML0248-A), Sah98 = Sahara 98175 (PTS CML0278-B). Polished thin sections (PTSs) are available at the Cascadia Meteorite Laboratory.
[b] Olivine predominant grain diameters, and approximate diameters of feldspathic areas, as observed in PTS.
[c] Pyroxene-rich object.
[d] Fine-grained Type I chondrule.
[e] Contains zoned, mostly ferroan olivine and magnesian pyroxene and appears to be transitional between Types I and II.

of traverses and targeted analyses in the objects. The composition of each DB-EMPA analysis was corrected for the unequal-density-effect (Nazarov et al., 1982; Warren, 1997) using the procedure of Warren (1997). Mineral proportions were calculated for each DB-EMPA analysis using a norm calculation that was tailored to minerals in ordinary chondrites. For comparison to AO and chondrule data, a version of the CWPI thermodynamic code (Petaev and Wood, 1998, 2005) was used to model equilibrium condensate compositions. All CI-normalized plots utilize the average CI chondrite data of Anders and Grevesse (1989). Plots showing elements arranged by condensation temperatures are based on the work of Lodders (2003), except that the relative order of condensation temperatures for Na and K were switched consistent with results from the CWPI code. Further details on experimental methods are given in the Appendix.

3. RESULTS

Textures of AO objects and possibly related chondrules are illustrated in Figs. 1–3, and petrographic and chemical data for these objects are given in Tables 1–3. Supplementary data are provided in an Electronic Annex (Appendix B) and include (1) petrographic and olivine EMPA chemical data for all 32 objects studied in detail (Table EA-1-1); (2) bulk chemical and normative compositions for objects based on DB-EMPA (Table EA-1-2); and (3) trace-element data (Tables EA-2-1 and EA-2-2).

3.1. Petrography

The objects studied show a range of textures (Fig. 1). They can be classified as (a) AO objects (Fig. 1a), (b) fine Type II chondrules (Fig. 1b), (c) coarse Type II chondrules (Fig. 1c), and (d) ultrafine matrix lumps (Fig. 1d). Characteristics of these objects are summarized in Table 1 and are described below.

3.1.1. AO objects

AO objects are composed of fine-grained ($\leqslant$5–10 μm-grain-diameter) ferrous olivine ($Fa_{12–35}$), troilite, pyroxene, feldspathic material, metal, and distinctly magnesian olivine ($Fa_{0.7–12}$) and pyroxene grains (Figs. 1a and 2). The magnesian grains are likely xenocrysts (relict grains) and are as identified as such both by their distinctive compositions and also by their coarser grain sizes and irregular grain shapes. Ferrous olivine grains show either no zoning or are zoned with magnesian cores. Troilite is commonly concentrated on object peripheries (Fig. 2a–f). AO objects often contain well-defined clumps of coarser material that have microporphyritic (in one cased, barred olivine) textures, which appear to be relict microchondrules (Fig. 2c, e and g). AO objects can form both inclusions and rims on chondrules (Figs. 2 and 3). We categorize AO objects into three transitional stages, including (a) unmelted AO objects (AO-U), (b) weakly melted AO objects (AO-WM), and (c) melted AO objects (AO-M).

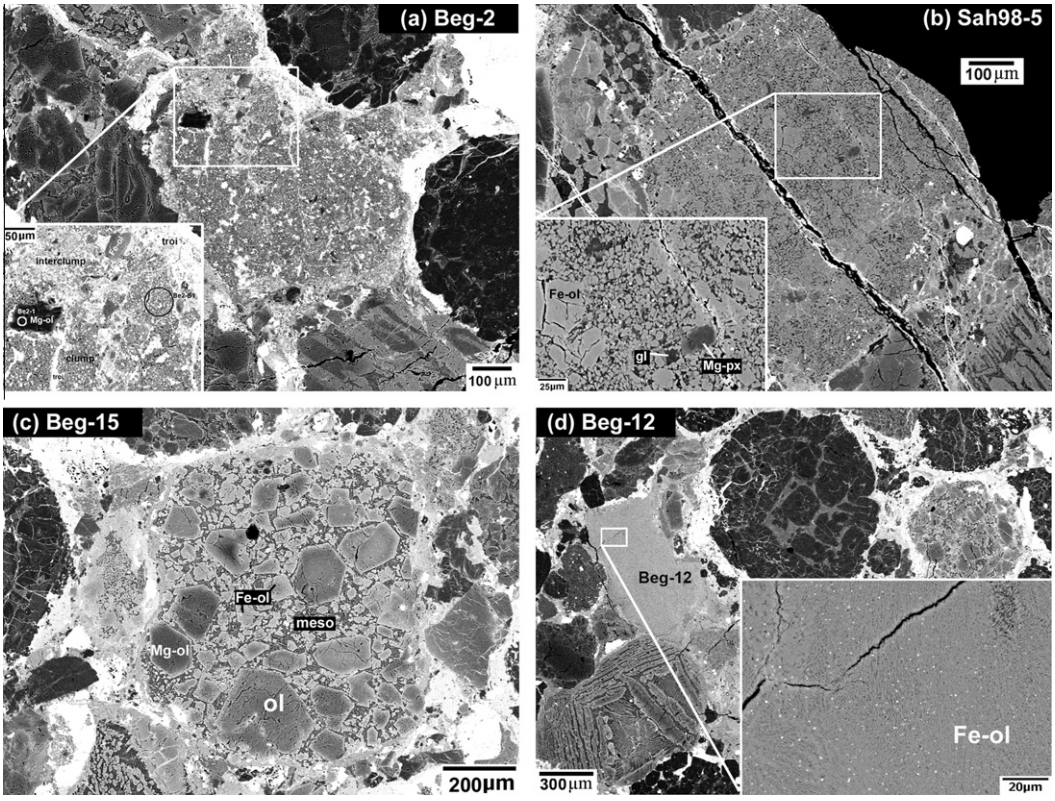

Fig. 1. BSE images showing examples of various types of objects. (a) AO object Beg-2. (b) Fine Type II chondrule Sah98-5. (c) Coarse Type II chondrule Beg-15. (d) Ultrafine matrix lump Beg-12. Circles in part a indicate SIMS analysis locations. Abbreviations: ol = olivine; troi = troilite; px = pyroxene; gl = glass; meso = mesostasis.

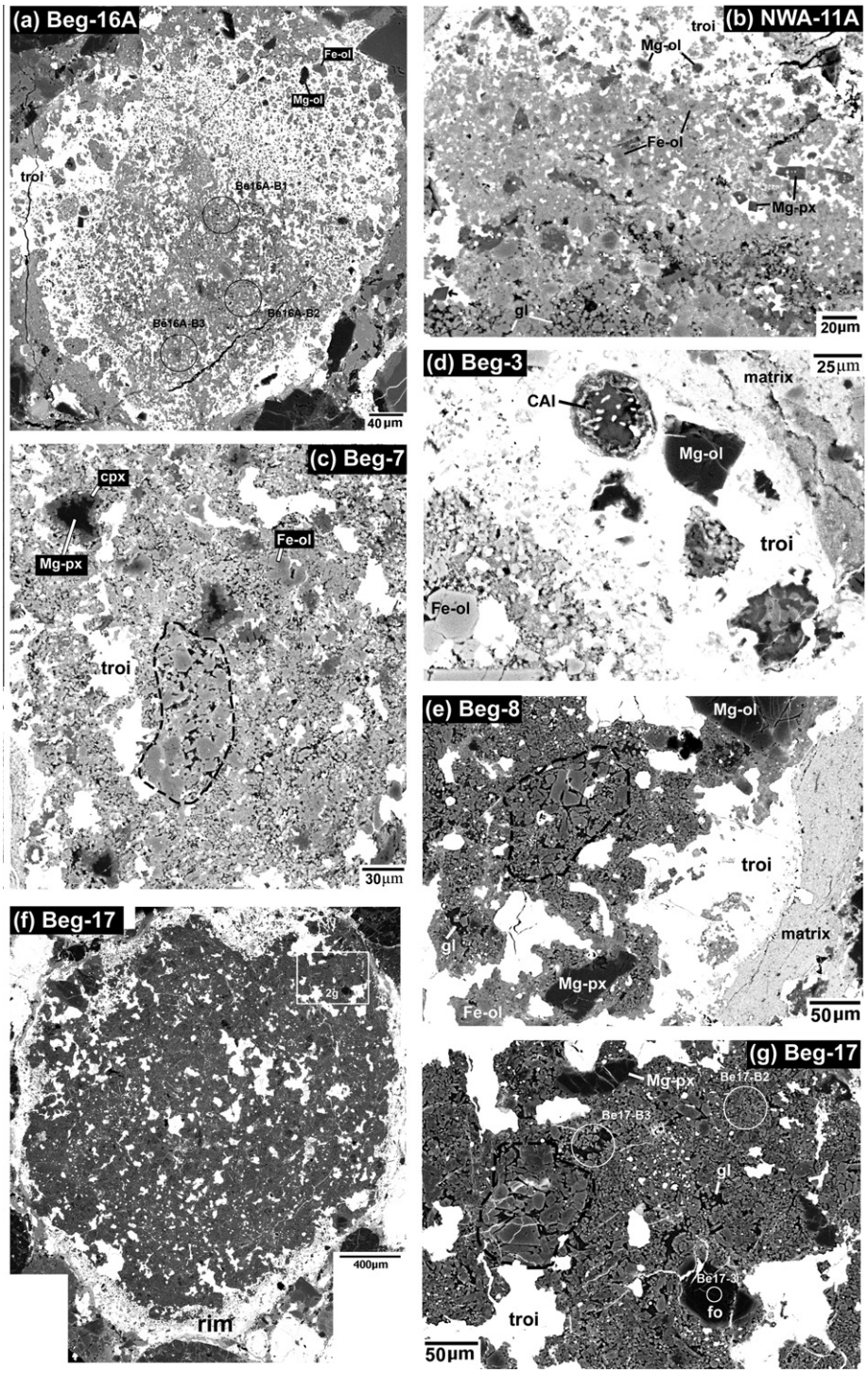

Fig. 2. BSE images of AO objects. (a) Beg-16A, a Type AO-U object containing a prominent troilite-enriched periphery composed of 'network troilite'. Circles show the locations of broad beam SIMS analyses. (b) NWA-11A, showing a thick AO-U rim between a fine Type II chondrule core (at bottom) and a troilite-enriched periphery (top). Some magnesian low-Ca pyroxene grains (Mg-px at right, arrow at lower left) have idiomorphic faces against troilite, as do Fe-ol grains (not visible in image). (c) Beg-7, an AO-WM object containing a relict chondrule (dashed line) and irregularly-shaped cores of magnesian low-Ca pyroxene (Mg-px) surrounded by coronas of augite (cpx). (d) Portion of AO-U object Beg-3, showing a CAI, forsterite clast, and other apparent fragments embedded in troilite along the edge of the object, and a portion of the interior containing fine and coarser grains (lower left). (e) Beg-8, an AO-M object showing a relict chondrule (dashed lines) and glass. (f) Beg-17 is a large AO-M object that contains a troilite-rich rim. The box shows the region magnified in part g. (g) Closer view of Beg-17 showing a relict chondrule (dashed lines), glassy mesotasis, and the locations of SIMS analyses (circles). Abbreviations as in Fig. 1.

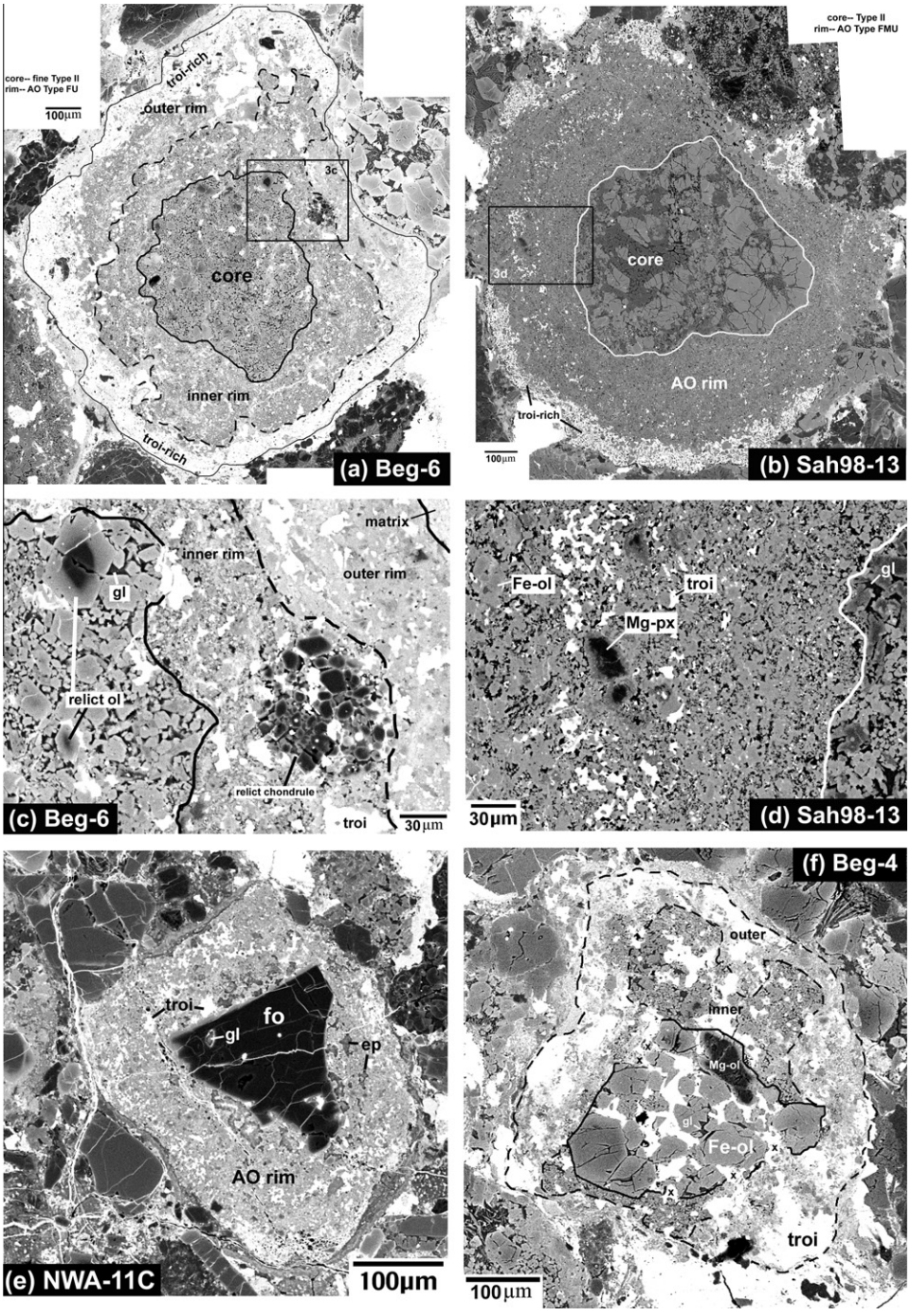

Fig. 3. BSE images of AO rimming features. (a) Beg-6 is a classic 'dark zoned object' that contains a fine Type II core surrounded by an inner and outer AO rim. Troilite is concentrated in the outermost portion of the outer rim. The box shows a region magnified in part c. (b) Sah98-13 contains a coarse Type II chondrule core surrounded by a thick AO rim. Troilite is concentrated in the outermost part of the rim. The box shows a region magnified in part d. (c) Close-up of Beg-6 showing the fine Type II core at left (with relict olivine grains), the inner AO-U rim which contains a relict Type I chondrule, and the outer AO-U rim that has a different texture. (d) Close-up of the AO-WM rim in Sah98-13, showing numerous feldspathic patches (dark spots), a partial concentric band of troilite, a relict grain of magnesian low-Ca pyroxene (Mg-px), and a portion of the coarse Type II core (extreme right). (e) NWA-11C contains an obvious accretionary AO-U rim that surrounds an angular forsterite grain. Glass inclusions occur in the forsterite. ep = epoxy in partially plucked areas. (f) Beg-4 has two different types of AO rims that surround a small coarse Type II chondrule core (with has a prominent relict Mg-ol grain). An outer AO-U rim largely surrounds the object; two patches of a coarser-grained inner AO-M rim are also present. Troilite has replaced mesostasis glass in the core. In a few locations (marked by x), troilite appears to cross over the edge of the core into the AO rim. Abbreviations as in Fig. 1.

Table 2
Bulk composition and norms of AO objects and Type II chondrules.[a]

Type	AOs, all types $N = 23$		Fine Type II $N = 9$		Coarse Type II[b] $N = 6$	
	Mean (s.d.)	Range	Mean (s.d.)	Range	Mean (s.d.)	Range
at.						
Mg#	0.72 (0.08)	0.51–0.87	0.70 (0.08)	0.61–0.85	0.70 (0.12)	0.47–0.84
Na/Al	0.49 (0.25)	0.11–0.91	0.28 (0.14)	0.16–0.56	0.20 (0.04)	0.14–0.24
S/Al	18.5 (30.8)	0.09–122	0.44 (0.34)	0.04–1.08	0.22 (0.20)	0.06–0.60
wt%						
SiO_2	27.2 (9.26)	7.88–42.7	36.8 (4.8)	29.3–46.9	38.9 (3.9)	32.9–45.0
Al_2O_3	1.69 (0.95)	0.33–4.62	2.15 (1.07)	0.86–4.57	2.55 (1.36)	1.23–4.79
Cr_2O_3	0.58 (0.35)	0.08–1.83	0.71 (0.23)	0.30–1.18	0.52 (0.11)	0.36–0.65
FeO	14.7 (6.5)	3.80–31.8	19.4 (5.3)	8.37–22.3	18.3 (4.8)	14.2–26.5
MnO	0.25 (0.07)	0.12–0.33	0.32 (0.06)	0.22–0.40	0.35 (0.06)	0.25–0.42
MgO	18.2 (5.4)	5.93–25.6	26.3 (4.5)	19.8–36.1	25.3 (7.7)	15.5–38.2
CaO	1.76 (1.27)	0.28–5.38	1.87 (1.09)	0.28–4.11	1.92 (1.31)	0.37–4.22
Na_2O	0.45 (0.28)	0.05–1.28	0.34 (0.19)	0.17–0.60	0.33 (0.22)	0.14–0.69
Ni	1.58 (0.95)	0.16–3.55	0.85 (1.08)	0.12–3.57	1.04 (1.32)	0.05–3.37
S	9.17 (7.72)	0.25–27.2	0.58 (0.51)	0.12–1.62	0.27 (0.14)	0.07–0.46
Cl	<0.01 (0.01)	<0.01–0.03	0.01 (0.01)	<0.01–0.03	0.01 (0.01)	<0.01–0.02
Fe (troilite)	15.9 (13.4)	0.43–47.4	1.01 (0.90)	0.21–2.82	0.46 (0.24)	0.12–0.81
Fe (metal)	3.67 (2.30)	0.40–8.82	2.19 (2.68)	0.30–8.87	2.08 (2.28)	0.13–5.32
Total	95.1 (3.5)	86.4–100.8	92.5 (2.5)	88.8–96.4	92.1 (3.6)	86.2–97.6
Norm (vol%)						
Olivine	48.7 (17.5)	18.9–91.6	66.5 (19.0)	28.4–89.9	57.6 (19.6)	23.2–82.1
Orthopx	10.7 (11.6)	<0.01–45.6	15.4 (13.9)	1.60–43.1	25.3 (10.8)	12.1–45.0
Clinopx	5.75 (4.70)	<0.01–18.4	4.54 (3.67)	0.13–10.4	4.08 (3.33)	0.57–9.48
Plagioclase	8.82 (4.36)	1.99–20.4	9.81 (4.54)	3.00–18.7	10.2 (6.36)	3.19–21.0
Sodalite	0.03 (0.07)	<0.01–0.27	0.08 (0.10)	0.02–0.32	0.10 (0.08)	0.02–0.22
Chromite	0.66 (0.41)	0.11–2.14	0.79 (0.25)	0.33–1.29	0.57 (0.12)	0.39–0.69
Metal	2.75 (1.78)	0.27–6.77	1.61 (2.32)	0.18–7.60	1.61 (1.84)	0.08–4.2
Troilite	22.6 (20.0)	0.54–71.5	1.27 (1.10)	0.25–3.48	0.58 (0.31)	0.16–1.0

N = number of objects averaged and included in range; s.d. = standard deviation; Orthopyx = low-Ca pyroxene (enstatite + ferrosilite); Clinopx = high-Ca pyroxene (diopside + hedenbergite); Chromite = $FeCr_2O_4$ + $MgCr_2O_4$; Metal = FeNi metal alloy. Norm adds to 100% within rounding error.

[a] Based on corrected defocused beam electron microprobe data. Totals are often low owing to pits and surface irregularities in the analysis volumes.

[b] Excludes Beg-4 and Beg-5 which have low, possibly unrepresentative, mesostasis fractions.

AO-U objects are composed mainly of anhedral olivine grains ⩽5 μm across and mostly lack feldspathic (possibly glassy) areas. Examples are Beg-16A (Fig. 2a), much of NWA-11A (Fig. 2b), and Beg-3 (Fig. 2d). All these objects contain 'network' troilite that compactly fills spaces between silicate grains, increasing in abundance towards the object edges. Beg-3 notably contains a layered micro-CAI, the only one found in our study, composed of a core of grossite ($CaAl_4O_7$) and perovskite (Fig. 2d).

AO-WM objects are composed mostly of anhedral–subhedral olivine grains ⩽5 μm across with a substantial proportion of feldspathic, possibly glassy domains (⩽1–5 μm wide). Examples include Beg-2 (Fig. 1a) and Beg-7 (Fig. 2c). Beg-7 contains some irregularly-shaped relict magnesian low-Ca pyroxene grains that have overgrowths (~5–10 μm wide) of augitic pyroxene (Fig. 2c). Similar high-Ca pyroxene (augite or pigeonite) overgrowths are seen in all AO object types, but they are not present in the chondrules we studied.

AO-M objects are slightly coarser (olivine grains ⩽10 μm in diameter) and show clear textural evidence for melting, with feldspathic glassy regions up to ~2–12 μm wide occurring interstitial to euhedral–subhedral olivine and low-Ca pyroxene grains. Examples include Beg-8 (Fig. 2e) and Beg-17 (Fig. 2f and g), the latter being the largest AO object observed (~2.5 × 3.0 mm across). Troilite in these inclusions tends to form more compact masses than the more distributed network structures in Type AO-U (compare Fig. 2f and a). Moreover, AO-M objects contain drop-formed masses of metal and troilite consistent with melting (Fig. 2g). Other objects similar to AO-M but containing more magnesian grains are present in the meteorites (e.g., Beg-9).

3.1.2. Type II chondrules

Type II chondrules have microporphyritic textures and come in two textural varieties, fine Type II and coarse Type II. These chondrules contain less troilite than the AO objects described above, but like them most are dominated by ferroan olivine and contain relict magnesian olivine and low-Ca pyroxene grains.

Table 3
Representative (col. 1–5, 7–8, 10–11) and average (6, 9, 12) trace element compositions of fine-grained multi-phase areas in AO objects and Type II chondrules determined by broad beam SIMS.

	Relatively unfractionated[1]						Incompatible-element-rich[2]			Ca-REE-poor[3]		
	(1)	(2)	(3)	(4)	(5)	(6)	(7)	(8)	(9)	(10)	(11)	(12)
Object	Beg-2	Beg-16A	Beg-17	Sah98-5	NWA-15	Mean (s.d.)	Beg-17	Beg-8	Mean (s.d.)	Sah98-5	Sah98-12	Mean (s.d.)
Type	AO-WM	AO-U	AO-M	Fine II	Coarse II		AO-M	AO-M		Fine II	AO-WM	
N	3	3	1	2	2	31	1	2	10	1	3	7
Analysis	a	b	Be17-B2	c	d		Be17-B3	e		S5-B3	f	
Na, mg/g	9.97	3.85	10.9	9.05	5.08	6.30 (3.60)	25.4	19.9	16.1 (6.1)	9.02	15.7	6.30 (3.60)
Mg, wt%	17.9	18.2	20.5	18.5	14.7	16.7 (3.0)	10.7	12.2	15.8 (3.3)	19.1	20.7	19.8 (1.9)
Al, wt%	1.32	0.931	1.78	1.70	1.93	1.34 (0.38)	3.72	2.16	2.24 (0.62)	1.84	1.87	1.76 (0.19)
Si, wt%	16.3	13.7	20.3	16.6	17.4	15.0 (2.4)	20.3	15.4	18.3 (2.5)	16.6	17.3	16.8 (1.6)
P, μg/g	1350	1440	478	980	1090	1090 (330)	500	1060	1020 (510)	1200	940	992 (117)
K, mg/g	1.37	0.432	1.60	1.57	0.595	0.868 (0.480)	3.51	2.47	2.30 (0.55)	1.60	1.90	1.66 (0.79)
Ca, wt%	1.12	1.27	1.32	1.42	1.53	1.14 (0.46)	1.73	1.02	1.54 (0.48)	0.525	0.238	0.350 (0.142)
Sc, μg/g	6.62	6.82	8.27	7.97	8.95	7.21 (1.56)	8.15	7.02	8.39 (0.85)	7.31	4.95	6.00 (1.29)
Ti, μg/g	601	581	744	641	896	631 (112)	1350	936	1010 (190)	466	496	513 (180)
V, μg/g	65.0	61.7	81.7	78.8	72.2	68.9 (28.3)	61.0	51.7	72.9 (16.1)	48.0	80.8	69.8 (36.8)
Cr, mg/g	3.46	3.42	3.50	3.63	3.11	3.39 (1.69)	2.82	2.26	3.51 (1.07)	2.28	3.91	3.62 (1.77)
Mn, mg/g	3.00	3.15	3.89	3.22	2.87	2.93 (0.54)	2.52	2.42	2.85 (0.37)	3.32	3.73	3.69 (0.90)
Fe, wt%	21.5	42.6	11.6	22.0	18.0	29.9 (14.9)	8.36	11.6	16.2 (6.2)	25.1	28.3	30.3 (12.0)
Co, mg/g	0.424	0.647	0.191	0.0935	0.129	0.886 (1.345)	0.508	0.290	0.329 (0.212)	0.0935	0.0868	0.113 (0.092)
Ni, mg/g	11.2	12.6	4.35	5.18	1.90	11.7 (10.9)	4.90	5.76	4.57 (3.98)	7.90	10.2	8.61 (2.81)
Rb, μg/g	6.44	1.30	n.d.	5.06	3.91	3.84 (1.93)	n.d.	6.62	6.68 (2.01)	3.83	3.64	3.76 (0.78)
Sr, μg/g	12.8	32.9	10.7	12.8	17.4	17.4 (10.1)	16.8	14.2	14.8 (6.0)	28.8	15.5	17.9 (7.1)
Y, μg/g	2.16	2.34	2.64	2.46	2.20	2.33 (0.46)	5.03	3.55	3.73 (0.92)	1.41	0.892	1.20 (0.38)
Zr, μg/g	7.29	7.68	8.34	8.46	12.7	8.35 (1.95)	17.0	11.6	11.9 (3.0)	8.89	7.11	7.58 (1.38)
Ba, μg/g	2.45	4.27	2.89	3.82	3.80	3.13 (1.37)	6.52	5.10	3.78 (1.86)	6.77	4.97	5.35 (1.26)
La, ng/g	295	296	310	270	318	289 (74)	815	535	581 (137)	212	164	189 (36)
Ce, ng/g	798	709	957	676	804	762 (168)	2020	1460	1490 (400)	516	371	450 (110)
Pr, ng/g	114	114	139	109	131	116 (27)	316	215	222 (58)	79.9	47.0	57.9 (12.6)
Nd, ng/g	531	543	653	533	598	555 (112)	1360	1010	1040 (260)	338	237	288 (62)
Sm, ng/g	163	157	193	210	200	170 (32)	415	293	311 (71)	79.5	65.2	76.7 (12.2)
Eu, ng/g	43.4	73.5	38.5	65.3	86.9	56.6 (21.3)	104	90.1	83.1 (19.6)	78.8	43.6	52.8 (14.0)
Gd, ng/g	151	181	283	264	250	217 (54)	623	424	425 (100)	128	68.7	97.5 (29.4)
Tb, ng/g	36.7	41.0	62.6	56.0	52.9	45.0 (8.3)	101	83.6	81.2 (17.1)	33.1	15.5	21.6 (6.7)
Dy, ng/g	334	287	398	370	384	340 (61)	815	600	600 (127)	191	115	154 (39)
Ho, ng/g	72.2	56.3	78.0	81.1	77.9	71.9 (17.7)	139	122	130 (27)	43.6	26.1	38.1 (13.2)
Er, ng/g	206	202	273	269	240	228 (39)	467	390	403 (70)	164	86.6	118 (33)
Tm, ng/g	26.7	27.7	44.7	40.0	37.1	34.1 (8.7)	78.4	58.4	57.7 (13.8)	25.0	11.3	18.2 (8.7)
Yb, ng/g	207	217	270	268	239	242 (40)	469	368	395 (67)	187	108	142 (50)
Lu, ng/g	37.2	37.9	74.6	44.8	44.6	41.2 (11.4)	80.2	61.6	65.0 (11.2)	37.3	20.7	26.7 (8.5)

a: Mean of analyses Be2-B1, Be2-B2, Be2-B3. b: Mean of analyses Be16A-B1, Be16A-B2, Be16A-B3. c: Mean of analyses S5-B2, S5-B4. d: Mean of analyses N15-B1, N15-B2. e: Mean of analyses Be8-B2, Be8-B3. f: Mean of analyses S12-B1, S12-B2, S12-B3. Abbreviations as in Table 2, also n.d. = not determined.

[1] Unfractionated pattern: individual analyses have mean lithophile element abundances of ~1.0–1.7 × CI chondrites with a coefficient of variation (CV) of 19–42%.

[2] IE-rich pattern: individual analyses have mean abundances of ~1.8–2.8 7 × CI, CV ~ 29–46%.

[3] Ca-REE poor pattern: individual analyses have 'a W' REE pattern, CV > 50%.

Fine Type II chondrules are dominated by euhedral–subhedral olivine grains ($Fa_{12–38}$) that range from ~5–60 μm but are mostly <25 μm across (Fig. 1b). Glass occurs interstitial to larger olivine grains, sometimes contains pyroxene crystallites, and is present in areas ⩽2–15 μm wide. Most such objects can be described as fine Type IIA or IIAB chondrules, but one object with $Fa_{4–6}$ olivine (the core of Beg-13) is better described as a fine Type IA chondrule, and another with magnesian pyroxene and zoned ferrous olivine (Sah98-4B, with bulk Mg# ~0.85) is better described as being transitional between fine Type II and fine Type I.

Coarse Type II chondrules have coarser olivine grains (10–250 μm across) and wider glassy regions (up to ~50 μm) (Fig. 1c). In the coarse Type II chondrules analyzed here, olivine grains tend to be zoned with ferrous rims and magnesian cores (range $Fa_{6.5–31}$) but are dominantly ferrous ($Fa_{>10}$). Beg-15 (Fig. 1c) is typical in most respects, except that it appears to contain many relict grains that did not crystallize *in situ*, as there is no correlation between olivine grain size and grain core forsterite content, a correlation that would be expected if all grains crystallized from the same parent melt.

3.1.3. Ultrafine matrix lumps

For comparison to AO objects and chondrules, we also studied two inclusions (Beg-12, Beg-17A) that are much finer-grained (grains ⩽1 μm across). These objects lack coarser material and in BSE images appear uniform (Fig. 1d). Beg-12 (Fig. 1d) is composed primarily of ferroan olivine; Beg-17A is composed primarily of ferroan low-Ca pyroxene. Both objects have irregular shapes and contain little sulfide. We term them ultrafine matrix lumps (Table 1). These objects are relatively uncommon and were found only in NWA 4910.

3.1.4. Rimming structures

AO objects of different types are present as rims (discrete outer portions) around fine Type II chondrules (Fig. 3a and c), coarse Type II chondrules (Fig. 3b, d and f), and coarse, isolated olivine grains (Fig. 3e). Contacts between the rims and core objects are relatively sharp in most cases (Fig. 3). AO objects that form rims around coarser objects are sometimes layered with sulfide-rich edges (Fig. 3a, b and f). Although AO-like rims typically surround ferroan core objects, they sometimes mantle magnesian cores, including fine Type I chondrules (Beg-13), transitional fine Type I–II chondrules (Sah98-4B), and individual forsterite grains (NWA-11C, Fig. 3e). No examples were found of AO material surrounding core objects more ferroan than the rims.

Some rims have more than one AO textural type. A good example of the latter is Beg-4 (Fig. 3f). For this object, an 'inner rim' of Type AO-M contains glass and is present as two lobes on opposite sides of the core, whereas an 'outer rim' of Type AO-U surrounds the entire object except in one location. Although the contacts between the core and two rim components are fairly sharp, troilite appears to extend across the core-outer rim contact in multiple locations (marked by 'x' in Fig. 3f). Troilite appears to have largely replaced the glassy mesostasis of the chondrule core (Fig. 3f). Besides Beg-4, two other objects (NWA-11 and Beg-16) show similar layered AO rims around Type II chondrules, with outer AO-U and inner AO-M rims. Two other objects (Beg-1 and Beg-17X) show textural evidence of sulfide from AO margins replacing the glassy mesostases of Type II chondrule cores.

3.2. Bulk chemistry

3.2.1. Major and minor element bulk chemistry and norms (DB-EMPA)

Table 2 presents average bulk compositions and norms for AO objects and Type II chondrules, and Table EA-1-2 and Fig. EA-1-1 in the Electronic Appendix provide data for individual objects. Different textural types of AO objects (Section 3.1) have similar bulk composition and norms; the same is true for fine Type II and Type II chondrules. However, AO objects (all three types) on the one hand, and Type II objects (fine and coarse) on the other, differ from one another chemically. Normative and bulk chemical data for major elements are plotted in Figs. 4 and 5.

Troilite abundance is highly variable, but on average, AO objects contain ~22 vol% normative troilite compared to ~1–2 vol% in Type II chondrules (Table 2). Most AO objects are enriched in troilite compared to bulk LL chondrites, whereas the opposite is true for Type II objects (Fig. 4a). The silicate normative mineralogy of both AO and Type II objects is highly variable but similar in terms of overall range and average composition (Fig. 4a–b, Table 2).

CI-chondrite-normalized data for average AO object and Type II chondrule bulk compositions are shown in Fig. 5. The data indicate that AO and Type II objects in these LL chondrites have compositions that are variations on a bulk LL chondrite composition. On average, AO objects are enriched in Fe, Ni, and (especially) S and slightly depleted in lithophile elements compared to LL chondrites (Fig. 5a). Although the average AO composition is low in Na compared to LL chondrites, some AO objects have a chondritic composition for all measured elements (e.g., Beg-2, Fig. EA-1-1). Both fine Type II and coarse Type II chondrules, in contrast, are clearly depleted in S and Na compared to LL chondrites and have lower S/Al and Na/Al values than AO objects (Table 2, Fig. 5b and c). Thus, AO objects are chemically like LL chondrites with additional Fe and S (troilite) and metal (Fe and Ni) components (diluting silicates and lithophile elements), whereas Type II objects are chemically like LL chondrites that are depleted in the most volatile elements (Na, S).

3.2.2. Trace element chemistry of multiphase areas (broad beam SIMS)

Representative and averaged trace element compositions based on SIMS analyses of multiphase fine-grained constituents in AO objects and Type II chondrules are given in Table 3 and shown in Fig. 6. Electronic Annex EA-2 provides more complete SIMS data as well as CI-normalized plots for some representative individual analyses (Tables EA-2-1 and EA-2-2, Fig. EA-2).

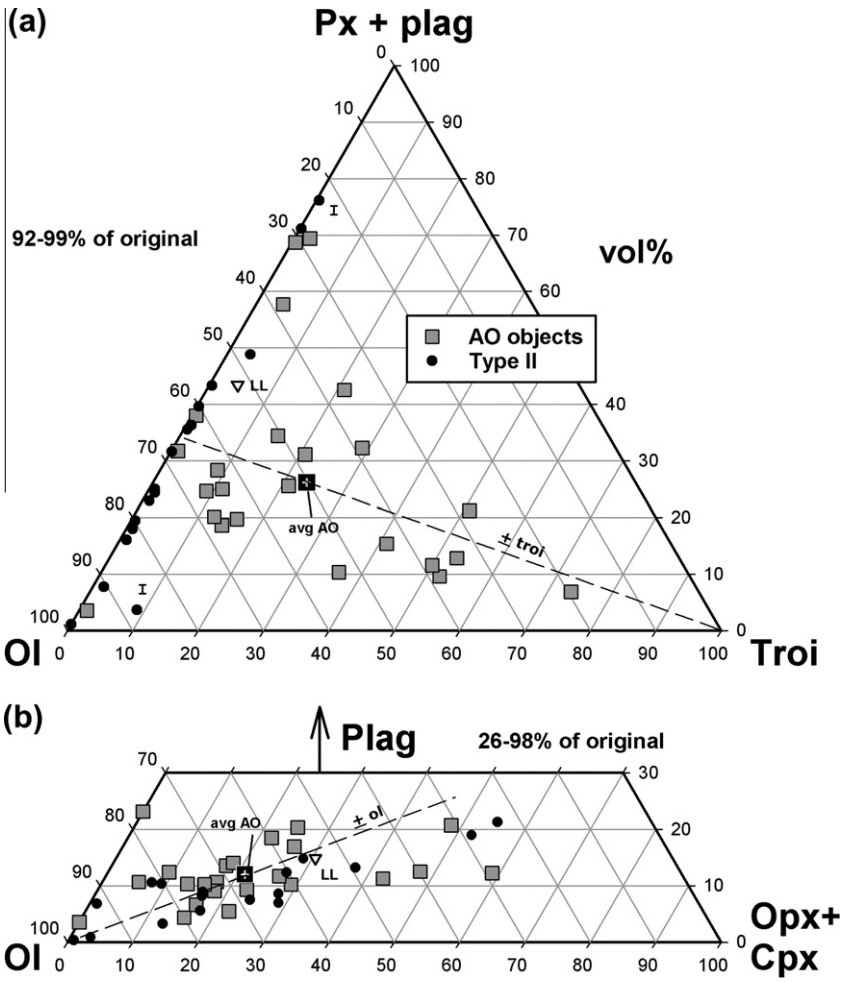

Fig. 4. Diagram illustrating the normative compositions of AO objects and Type II chondrules. The mean compositions of AO objects (this study) and LL chondrites (Jarosewich, 1990) are indicated. Abbreviations as in Fig. 1, and also plag = plagioclase; cpx = Ca-rich pyroxene; opx = low-Ca pyroxene; 'I' refers to objects better described as Type I or transitional Types I–II. (a) Ol–troi–(px + plag). A troi variation line through mean AO composition is shown for reference. The components shown represent 92–99% of the original total, with metal being the main missing component. (b) Ol–plag–(opx + cpx). An ol variation line through mean AO composition is shown for reference. The components shown represent 26–98% of the original total, with troilite being the main missing component.

Trace element compositions for fine-grained constituents display four different patterns. These can be characterized as (1) relatively unfractionated; (2) fractionated, incompatible element (IE)-enriched; (3) fractionated, Ca-REE-poor; and (4) fractionated, ultrafine lumps (Table 3, Fig. 6).

Relatively unfractionated patterns are most common for the fine-grained areas of AO objects (Fig. 6a). Similar patterns were also measured for fine-grained areas in some fine Type II chondrules and one coarse Type II chondrule (NWA-15). Lithophile element abundances for relatively unfractionated areas in AO and Type II objects average $1.38 \pm 0.19 \times$ CI chondrites (mean and standard deviation, based on 31 analyses) (Fig. 6a). This is essentially identical to that of whole-rock ordinary chondrites (Kallemeyn et al., 1989; Lodders and Fegley, 1998), suggesting a chondritic overall composition.

IE-enriched patterns are characterized by enrichments in incompatible elements, including especially the REE, alkalis, Zr, Y, Al, and Ti (Fig. 6b). More compatible elements, including Mg, V, Cr, Mn and Sc, are not enriched. Such patterns were obtained only for objects that contain glass in significantly large areas, namely AO-M objects and Type II chondrules, and not for AO-U or AO-WM objects. Clearly, the IE-enrichments can be explained as the result of igneous processes that resulted in a melt, which solidified as a glass analyzed by SIMS.

Fractionated, Ca-REE-poor signatures were obtained for some analyses of AO objects and fine Type II chondrules in Sahara 98175. These patterns are characterized by a 'W-shaped' REE pattern with relatively low abundances of REE except for a positive Eu anomaly, and large depletions in Ca and Co (Fig. 6c). A smaller depletion occurs for Y (Fig. 6c). As this pattern is seen only in Sahara 98175 (subtype 3.5) and not in the other two meteorites (subtype 3.1), it likely reflects a metamorphic effect. For this pattern, most elements that are relatively depleted (REE, Ca, Y) are known to partition in apatite, with equilibrium REE patterns for apatite being 'M' shaped (i.e., high middle REE contents with a negative Eu anomaly) (e.g., Watson and

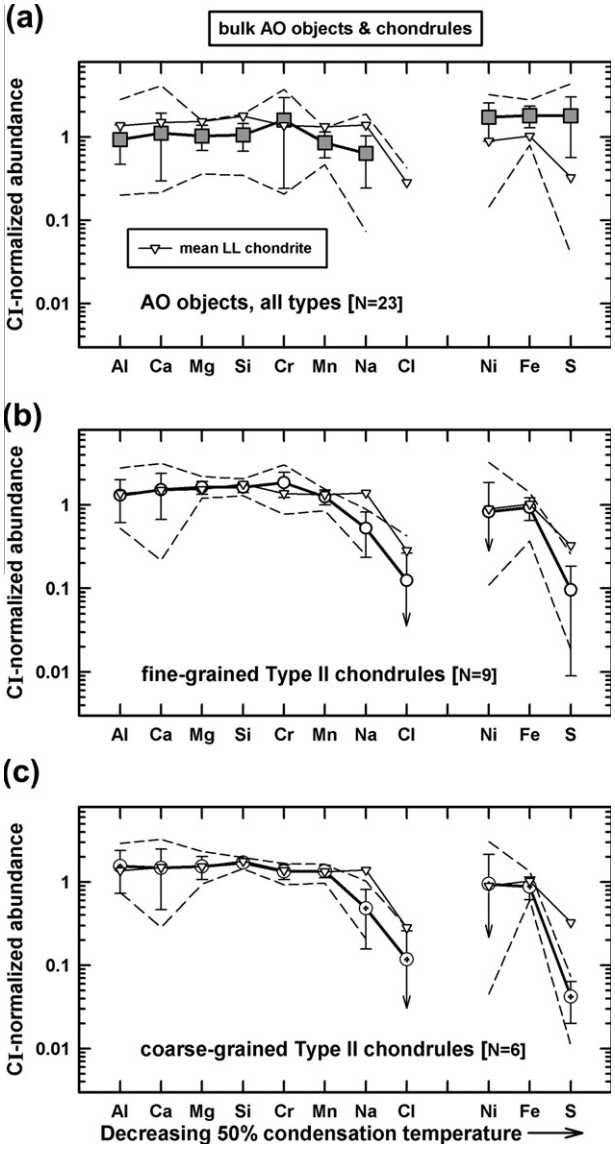

Fig. 5. CI-chondrite-normalized abundances for (a) AO objects, (b) fine Type II chondrules, and (c) coarse Type II chondrules, based on DB-EMPA data. Points show means, bars show standard deviations of the means, dashed lines indicate ranges. N = number of objects averaged. The mean LL chondrite composition is based on data from Jarosewich (1990).

Green, 1981; Fujimaki, 1986). The 'M' REE pattern is complementary to the 'W' pattern observed in the Sahara analyses. For AO objects and Type II chondrules, we suggest that metamorphic heating devitrified phosphate, which sequestered REE, Ca, Y, and possibly Co, depleting these elements elsewhere to give the observed Ca-REE-poor pattern.

The *fractionated, ultrafine lump pattern* obtained for lumps Beg-12 and Beg-17A is characterized by large fractionations, including enrichments in Mn and strong depletions in Ni, Co, and P (Fig. 6d). Moreover, Beg-12 has low abundances for Ca and Sr, and Beg-17A has low abundances of alkalies and Ba. The highly fractionated compositions of these fine matrix lumps are very different than the relatively unfractionated compositions often obtained in AO objects and fine Type II chondrules, implying no simple genetic relationship between the lumps and the other objects.

3.3. Mineral chemistry

3.3.1. Major and minor element olivine chemistry (EMPA)

AO and Type II objects contain olivine with similar major and minor element compositions. The average Fa contents of the ferroan olivine grains (excluding magnesian relict grains) are similar: for AO objects it is Fa 21.4 ± 7.0 (mean and standard deviation, based on 45 analyses in 12 objects), and for Type II objects it is Fa 20.3 ± 6.6 (based on 129 analyses, 17 objects). Cr_2O_3, MnO, and CaO contents in olivine also show similar distributions in AO objects and Type II chondrules (Fig. 7). Olivine in both object types shows: (a) maximum chrome contents at intermediate Fa values ($\sim Fa_{14-24}$) (Fig. 7a); (b) a positive correlation between MnO and Fa contents (Fig. 7b); (c) a similar scatter pattern in a CaO–Fa variation diagram (Fig. 7c); and (d) evidence for the same three chemical populations of olivine in a CaO/MnO vs. Fa plot (Fig. 7d). The populations include: (1) a low-Fa, high-CaO/MnO, low-Cr_2O_3 'refractory' population that often forms relict grains in the ferroan objects; (2) a 'main' population with intermediate Fa and intermediate CaO/MnO values and relatively high Cr_2O_3 contents; and (3) a 'refractory-poor ferroan' population with high-Fa, low-CaO/MnO, and low-Cr_2O_3 values (Fig. 7). In the classification scheme of Sears et al. (1992, 1995), these three populations correspond to chondrule classes (1) A1 and A2; (2) A3, A4, B1 and B2; and (3) A5 and B3, respectively. Altogether, olivine compositions obtained with EMPA suggest a close relationship between AO objects and Type II chondrules.

3.3.2. Trace element mineral chemistry (SIMS)

Trace-element compositions for olivine and low-Ca pyroxene in AO and Type II objects are given in Table 4 and shown as CI-normalized abundances in Fig. 8. Analyses are limited owing to fine grain size, and those for AO objects reflect atypically coarse grains (>15 μm across) in the objects. In Fig. 8, elements are arranged according to volatility (50% condensation temperatures) for cooling-insensitive elements, and according to cooling-rate-sensitivity (CRS) for cooling-sensitive (CS) elements (Ruzicka et al., 2008). This acknowledges that olivine and low-Ca pyroxene which are grown from rapidly cooled (i.e., 2000°C/h) melts have elevated concentrations of CS elements that reflect disequilibrium (Kennedy et al., 1993).

Fig. 8a shows no obvious differences in the trace-element composition of olivine in different types of objects, although an isolated forsterite grain (the core object of NWA-11C, analysis N11C-1) forms a distinctive endmember enriched in refractory lithophile elements (Sc, Y, Al, Ti, Ca), depleted in volatile lithophile elements (Cr, P, Mn, Rb), and depleted in siderophile elements (Ni, Co). For all olivine analyses, there is a tendency for the abundances of CS elements (Na-La) to increase with CRS (Fig. 8a). The data imply that coarser olivine grains in AO objects, fine Type II chondrules, and coarse Type II

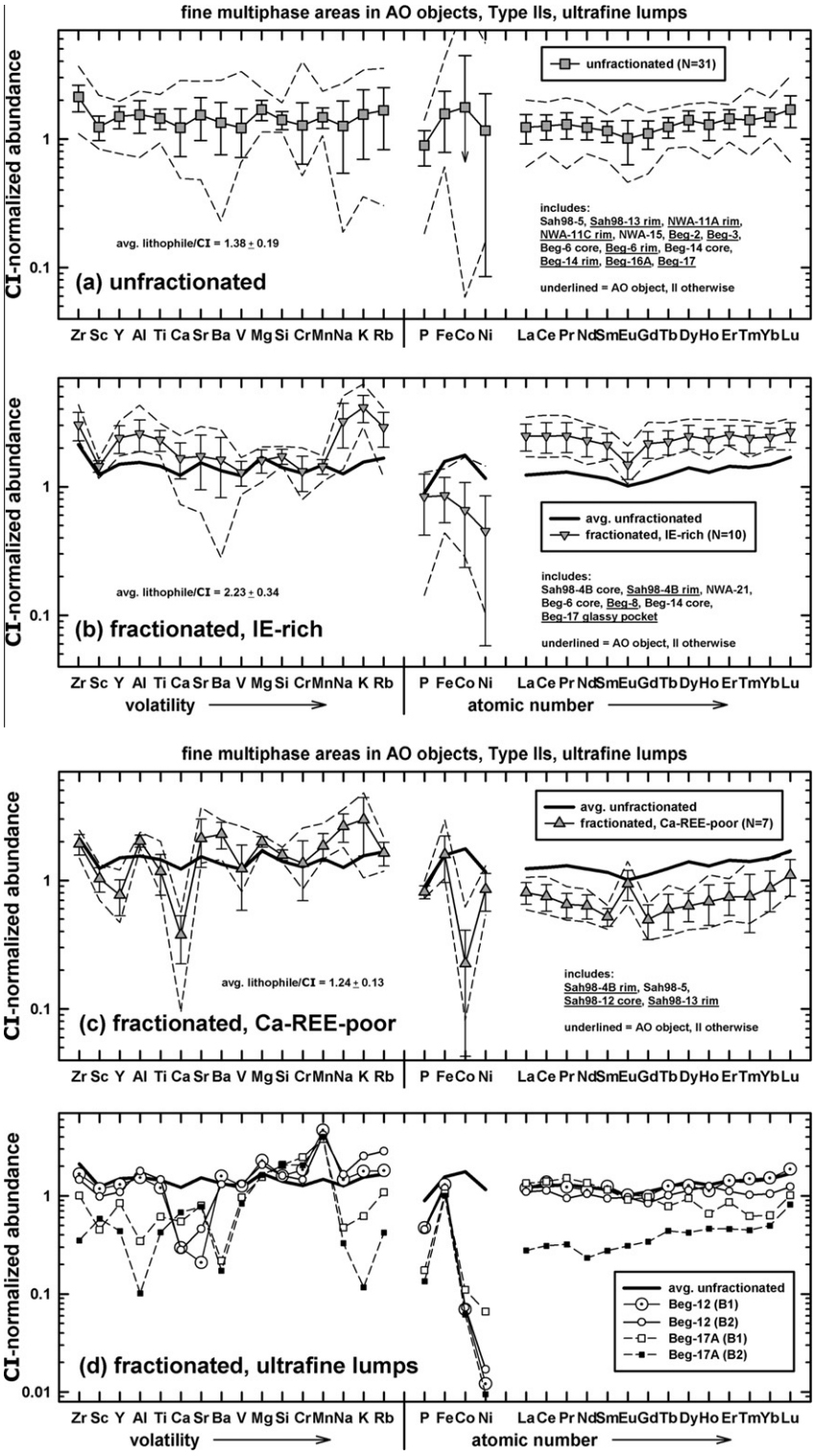

Fig. 6. CI-chondrite-normalized abundances for fine-grained multiphase areas in AO objects, Type II chondrules, and ultrafine matrix lumps, based on broad beam SIMS data. (a) Analyses of 'unfractionated' areas are characterized by lithophile mean abundances of ~1–1.7 × CI chondrites with a coefficient of variation among different lithophile elements of 19–42%. (b) Analyses of 'fractionated, incompatible-element-rich' (IE-rich) areas are characterized by lithophile mean abundances of ~1.8–2.8 × CI with a coefficient of variation among different lithophile elements of 29–46%. (c) Analyses of 'fractionated, Ca-REE-poor' areas are characterized by a 'W'-shaped REE pattern, generally low abundances of REE, Ca, and Co, and a coefficient of variation among different lithophile elements of >50%. (d) Analyses of 'fractionated, ultrafine matrix lumps' show fractionated abundances in lumps, with a coefficient of variation among lithophile elements of >50%. Parts a–c show averaged data (points indicate means, bars indicate standard deviations, dashes indicate ranges, N = number of analyses averaged), whereas part d shows individual analyses.

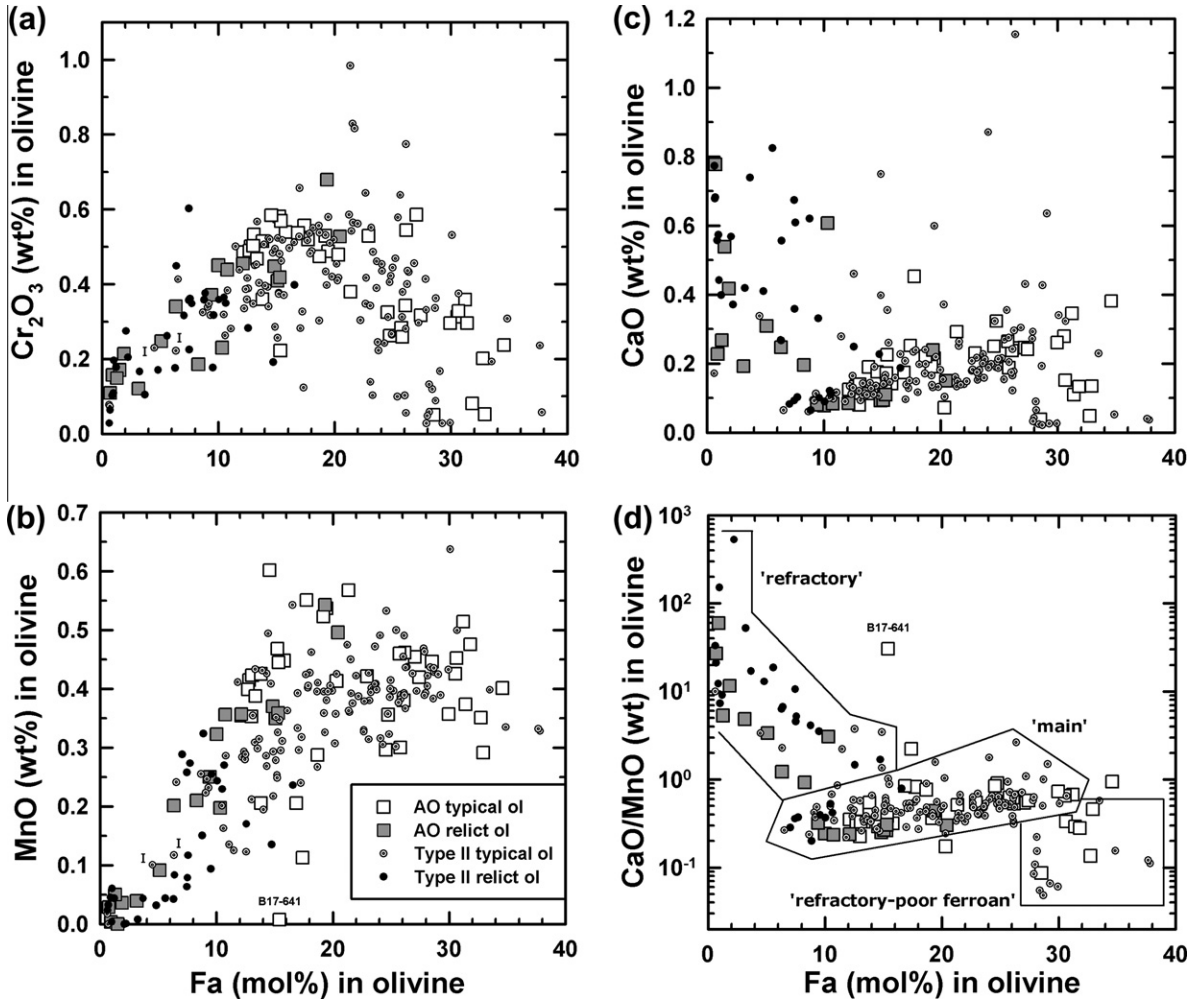

Fig. 7. Variation diagrams for minor element and Fa contents of olivine in AO objects and Type II chondrules. (a) Cr_2O_3 vs. Fa, (b) MnO vs. Fa, (c) CaO vs. Fa, (d) CaO/MnO vs. Fa. Most analyses with Fa < 10 are for relict grains. 'I' refers to objects better described as Type I or transitional Types I–II. Analysis B17-641 has anomalously low MnO which may be in error.

chondrules experienced broadly similar igneous and cooling histories. Most likely, the coarser olivine grains in AO objects represent chondrule debris.

Data for low-Ca pyroxene show that relict grains in AO-U object Beg-3 and AO-M object Beg-8 have similar compositions, whereas low-Ca pyroxene in Type II chondrule Sah98-13 has higher abundances of most trace elements (Fig. 8b). CI-normalized abundances of CS elements in low-Ca pyroxene from the two AO objects generally increase with CRS, whereas this pattern is not evident in the Type II chondrule (Fig. 8b). This could indicate that an igneous signature of rapid cooling is preserved for the two AO grains from NWA 4910 (LL3.1), but not for the presumably more metamorphosed chondrule grain from Sahara 98175 (LL3.5).

4. DISCUSSION

4.1. Dust accretion and heating to form AO objects

Our data support the conclusions of previous researchers that AO objects represent little-melted agglomerates of diverse components (Weisberg and Prinz, 1994, 1996). Textures suggest that AO objects contain both relict grains as well as fragments of small chondrules (Section 3.1), and mineral-chemical evidence strongly suggests that larger olivine and low-Ca pyroxene grains in AOs are chondrule debris (Section 3.3). AO objects that enclose ('rim') chondrules and coarse mineral grains (Section 3.1.4) are clearly accretionary in origin, and generally resemble previously described 'matrix-like rims' or 'dark rims' on chondrules (Ashworth, 1977; Allen et al., 1980; King and King, 1981; Metzler et al., 1992; Metzler and Bischoff, 1996). Agglomeration of AO material evidently followed previous episodes of chondrule formation and fragmentation and post-agglomeration heating episodes were of insufficient intensity to obliterate the identity of the various coarse components in AO objects.

Trace-element data suggest that the fine-grained multiphase fraction in AO objects has a near-chondritic composition on average (Section 3.2.2). Moreover, some AO objects have essentially chondritic bulk major and minor-element compositions, although overall bulk and silicate compositions for AOs are variable (Section 3.2.1).

Table 4
Representative composition of olivine (1–7) and low-Ca pyroxene (8–10) in AO objects and chondrules determined by narrow beam SIMS.

	Olivine							Low-Ca pyroxene		
	(1)	(2)	(3)	(4)	(5)	(6)	(7)	(8)	(9)	(10)
Object	Beg-2	Beg-6 rim	Beg-17	NWA-11A	NWA-15	Sah98-13 core	NWA-11C core	Beg-3	Beg-8	Sah98-13 core
Type	AO-WM	AO-U	AO-M	Fine II	Coarse II	Coarse II	IOG[b]	AO-U	AO-M	Coarse II
Analysis	Be2-1	Be6-1	Be17-4	N11A-1	N15-2	S13-B5	N11C-1	Be3-1	Be8-2	S13-3
Fa, mol%[a]	3.1	20.3	10.0	23.1	18.0	28.1	0.6	Fs 2.9	Fs 6.3	Fs 17.5
Na, mg/g	0.151	0.0500	0.0430	0.155	0.120	0.252	0.0880	0.388	0.696	4.12
Mg, wt%	25.9	27.2	24.8	26.8	n.d.	25.7	26.2	18.2	16.9	15.3
Al, mg/g	0.485	0.347	0.230	0.309	0.476	0.321	1.60	2.39	1.96	6.87
Si, wt%	19.1	17.8	18.8	17.5	18.0	17.6	19.5	27.1	26.8	26.4
P, μg/g	449	163	65.9	441	148	72.7	38.0	94.4	124	302
K, mg/g	0.0310	0.0270	0.0180	0.0250	0.0430	0.0510	0.0687	0.0990	0.0990	0.285
Ca, mg/g	1.42	0.633	0.410	1.48	0.888	0.392	3.51	1.62	1.61	13.4
Sc, μg/g	3.08	2.93	1.13	4.77	2.91	2.30	9.22	2.88	2.07	8.43
Ti, μg/g	58.9	29.2	21.8	34.2	24.8	22.2	304	127	127	331
V, μg/g	35.0	54.0	57.2	44.1	47.9	9.82	35.8	58.1	51.3	91.6
Cr, mg/g	1.24	3.41	3.07	2.87	3.71	0.501	0.622	2.64	2.85	6.16
Mn, mg/g	0.812	4.32	2.50	3.45	2.77	4.00	0.0378	0.833	1.43	3.87
Fe, wt%	10.8	15.5	5.54	15.2	9.82	18.7	0.459	3.46	2.55	6.97
Co, mg/g	0.438	0.204	0.189	0.153	0.0820	0.0411	0.00866	0.361	0.220	0.108
Ni, mg/g	6.75	3.78	2.74	0.472	0.333	0.731	0.251	5.14	2.99	1.66
Rb, μg/g	n.d.	0.913	0.174	0.418	0.205	0.624	0.101	0.994	0.974	1.59
Sr, μg/g	3.78	0.371	0.301	0.318	0.148	0.300	0.192	1.43	0.533	2.77
Y, ng/g	243	185	65.3	91.3	83.5	50.2	485	174	366	1006
Zr, ng/g	670	356	181	154	167	621	825	569	904	3120
Ba, ng/g	597	407	682	66.2	85.5	347	103	1410	1010	663
La, ng/g	77.8	101	40.2	51.5	45.4	104	53.2	89.2	97.8	169
Ce, ng/g	80.7	88.0	34.4	61.3	19.6	64.6	24.8	118	170	449
Pr, ng/g	16.3	24.5	13.8	9.50	11.9	20.7	12.4	20.5	33.5	49.4

Abbreviations as in Table 3.
[a] Determined by EMPA.
[b] Coarse, isolated olivine grain.

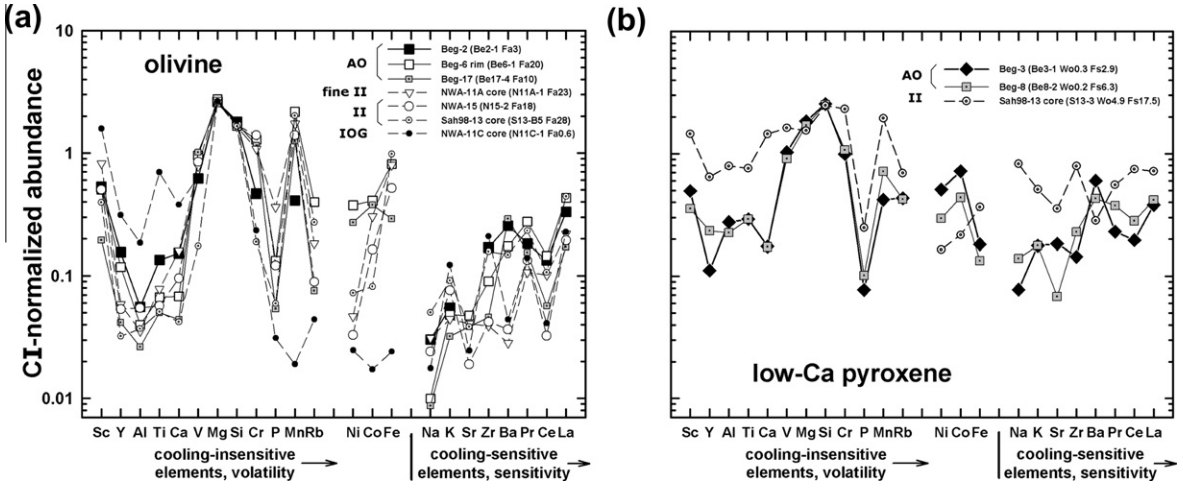

Fig. 8. CI-chondrite-normalized abundances for SIMS analyses of (a) olivine and (b) low-Ca pyroxene in AO objects, Type II chondrules, and an isolated olivine grain (IOG).

As the average AO bulk composition is enriched in S, Fe, and Ni and slightly depleted in lithophile elements compared to average LL chondrite (Section 3.2.1), AO objects can be regarded as mechanical mixtures of (a) fine silicate dust of essentially chondritic composition, (b) variable amounts of larger mineral and lithic components (including chondrule-derived xenocrysts of olivine and pyroxene and lithic debris), and (c) additional troilite and metal.

AO objects show evidence for having been variably heated, ranging from apparently sintered (Type AO-U), to slightly melted (Type AO-WM), to more substantially melted (Type AO-M). Evidence for such a transitional heating sequence is summarized below.

(1) AO-U objects show little evidence for silicate melting, although like other AO objects they are relatively compact. This implies that the original porosity one might expect for loosely accreted material was reduced by sintering.
(2) AO-WM objects show textural evidence suggesting that they were weakly melted. These objects contain many discrete feldspathic areas that might be amorphous and some olivine grains with subhedral morphologies (Section 3.1.1). Idiomorphic faces for olivine are most prominent where the olivine is in contact with feldspathic areas. This implies that melting occurred in AO-WM objects but that it was largely limited to feldspathic areas.
(3) Clinopyroxene (pigeonite, augite) overgrowths on irregularly-shaped magnesian low-Ca pyroxene relict grains are a distinctive feature found in various types of AO objects but were not observed in Type II chondrules (Section 3.1.1). As they are sometimes found in AO-U objects that were not melted appreciably and are most prominently observed in AO-WM objects that were slightly melted, such overgrowths may be coronas that formed by metamorphic reaction/growth during low degrees of melting.
(4) AO-M objects show textural features indicative of melting, such as the presence of glass, euhedral–subhedral grain morphologies for olivine and pyroxene, and the presence of compact forms for troilite and metal, including drop-shaped masses (Section 3.1.1; see also Weisberg and Prinz, 1996). AO-M objects have textures similar to those illustrated for 'coarse-grained' or 'igneous rims' on chondrules, which may have originated by the melting of matrix-like rims (Rubin, 1984; Krot and Wasson, 1995). The observations imply that AO-M objects experienced heating sufficiently intense to partly melt all the major phases within them.
(5) The incompatible-element-rich (IE-rich) trace element pattern found for some SIMS analyses in AO-M objects resemble those observed in Type II chondrules and suggests the existence of melt zones on a relatively large scale (i.e., a significant fraction of a ~40–50 micron broad SIMS beam) (Section 3.2.2). Conversely, the lack of IE-rich patterns for AO-U and AO-WM objects imply that melting effects in these objects, if any, were much more limited in spatial extent.
(6) The tendency for olivine grains to be coarser in AO-M objects that were significantly melted, compared to AO-U and AO-WM objects of similar composition that were less melted, implies olivine coarsening by crystallization from a melt.

4.2. Origin of troilite-rich margins in AO objects

A prominent feature of many AO objects is the concentration of troilite on the peripheries of the objects (Section 3.1.1). We infer that this reflects the late addition of S to the objects to form an S-rich melt.

A key observation is that in areas of AO objects that have the highest troilite contents, troilite forms a continuous network with embedded silicates (e.g., Fig. 2a and d). The texture cannot be explained simply by the accretion of troilite grains, as this process would not produce a continuous network of the mineral. Equilibrium condensation models for the solar nebula predict that troilite forms by reaction between metal and H_2S gas (e.g., Wood and Hashimoto, 1993; Ebel and Grossman, 2000; Lodders, 2003), but there is no evidence that troilite formed by this reaction in AO objects. No remnant, corroded metal is found, even away from the edges of AO objects, and it is unlikely that network troilite formed by complete conversion of metal to troilite.

The textures of troilite-rich peripheries in AO objects are instead more consistent with troilite forming from a fluid (gas, liquid) that was easily able to penetrate between silicate grains. Some AO-U objects that show no evidence for silicate melting contain network troilite rims (Fig. 2a and d), implying that this texture was produced while silicates were solid. In some objects with Type II cores surrounded by AO rims, troilite appears to be replacing the glassy mesotases of the cores (Section 3.1.1, Fig. 3f). This could indicate replacement of silicate melt by an S-rich liquid that crystallized to troilite.

There are two viable possibilities for producing an S-rich melt on the margins of AO objects, namely by (a) direct condensation to liquid under strongly non-canonical nebular conditions, or (b) melting previously formed sulfide grains. Although sulfide melts are not explicitly predicted by condensation models (owing to a limitation of the models), such melts might be stable nebular condensates under high pressure, oxidizing conditions (Ebel and Grossman, 2000). In this case, the troilite could be a direct gas-to-liquid condensate, and the concentration on the peripheries of objects can be explained by reaction between AO objects and an S-rich gas. This scenario is supported by considering the relationship between AO objects and chondrules (Section 4.3). Iron to make troilite could have been supplied from a melt within the objects or from a vapor. Alternatively, the troilite in AO objects could reflect heating processes sufficiently intense to melt troilite that was initially present in AO objects. In this case, heating of previously assembled metal and sulfide grains could form a eutectic S-rich melt even in the presence of solid silicates. Pressures might need to be relatively high to allow a sulfide liquid to be stable (Ebel and Grossman, 2000). However, it is not obvious why melting of pre-existing grains would result in troilite concentrations at object peripheries, unless it reflects an original zonation in the objects (initially more troilite or troilite + metal towards the outside), likely reflecting late addition of S to the objects.

We note that a troilite-rich object and some chondrule rims in Bishunpur (L3.1) with network textures similar to

those of AO objects were studied by Kojima et al. (2003), who argued that troilite crystallized from S-rich shock melts, which were derived from matrix troilite and driven into chondrule rims by shock waves, which also disrupted the parent body. We consider this model highly unlikely for AO objects as (1) it does not explain why characteristic shock-produced veins, shock melt pockets, or other evidence for strong shock are entirely missing from AO objects; (2) it does not explain how concentric layering structures in AO objects could be preserved during an intense shock disturbance; (3) it does not plausibly explain why troilite should be concentrated in AO objects and not in the more voluminous chondrules; and (4) it does not plausibly explain why AO objects should be more enriched in troilite than bulk chondrites.

4.3. Relationship between AO objects and Type II chondrules

Our data suggest that AO objects are transitional to Type II chondrules and that progressive heating of AO objects resulted in Type II chondrules, in a process involving both grain coarsening and evaporative melting. This supports the conclusions of various researchers that coarsening and evaporation could have been important during chondrule formation (Weisberg and Prinz, 1994, 1996; Hewins et al., 1996, 1997; Hewins, 1997).

There is a textural continuum grading from AO objects through fine and coarse Type II chondrules that extends the sequence shown within different types of AO objects. In this sequence, the textural changes include: (1) an increase in olivine grain size, (2) more prevalent euhedral and subhedral shapes for olivine grains, (3) larger areas of glassy mesostases, and (4) better development of microporphyritic textures (Section 3.1). These changes can be explained by melting and subsequent crystallization processes, which allowed fewer but coarser grains to crystallize from incomplete melts at the expense of finer-grained precursors. Experiments are consistent with this type of coarsening process and suggest that multiple heating events would be needed to make Type II chondrules from finer-grained AO object-like precursors if peak heating times were short (~1 min) (Hewins and Fox, 2004).

Bulk chemical data indicate that AO objects and Type II chondrules have significantly overlapping compositions, except that AO objects are usually strongly enriched in S, somewhat enriched in Fe, Ni, and have higher Na/Al values (Section 3.2). We suggest that partial loss of S and Na during evaporative heating resulted in the lower contents of these elements in Type II chondrules. The complementary S abundances for Type II chondrules (subchondritic) and AO objects (often superchondritic) (Fig. 5) can be explained by heating of dust of chondritic composition: S that was driven out of Type II chondrule melts could have been incorporated into coexisting AO objects, which were less strongly heated and therefore acted as cold traps. To account for the high Fe and Ni contents in AO objects and the textures of troilite (Section 4.2), we suggest that AO objects incorporated a metallic melt condensate that would have been enriched not only in S but also in Fe and Ni. Neither Fe nor Ni are especially volatile elements, so both would tend to concentrate in a condensed phase such as melt.

4.4. Formation conditions for AO objects and Type II chondrules

As the silicate solidus for chondrules is estimated as ~1300–1500 K (Connolly et al., 2006), melted AO objects (Types AO-M and AO-WM) and Type II chondrules must have been heated to peak temperatures (T_{max}) no less than this. Type AO-U objects were probably heated to temperatures below the silicate solidus but above the sulfide-metal eutectic (>1262 K), i.e., with T_{max} ~1260–1500 K.

To place further constraints on AO object and Type II chondrule formation conditions, we used the CWPI thermodynamic code (Petaev and Wood, 1998, 2005) to vary pressure (P), temperature (T), and system composition and compare model results to observations. Although objects that contain zoned or relict grains cannot be in complete equilibrium, relatively homogeneous fine-grained olivine is prevalent in most AO objects and Type II chondrules, suggesting that the fine-grained portions of these objects approached an equilibrium condition. As the fine-grained precursor material to AO objects and Type II chondrules appears to have been quasi-chondritic on average (Section 4.1), we modeled equilibrium evaporation (or sublimation) of a CI-chondrite-like (solar or 'cosmic') precursor under a variety of plausible nebular pressures (10^{-3}–10^{-6} bar), temperatures (2500–350 K), and effective 'dust/gas' (D/G) ratios. The latter were calculated according to the general procedure of Wood and Hashimoto (1993), which assigns elements to different nebular fractions (gas, dust, ice, tar). Values of D/G >1 (×cosmic) represent systems enriched in vaporized dust, which is the most effective way to achieve ferroan silicates (Wood and Hashimoto, 1993; Ebel and Grossman, 2000). Although models are presented for a CI-like precursor, similar results would be obtained assuming other types of chondritic precursors such as LL chondrite.

Fig. 9 shows the bulk compositions of AO and Type II objects compared to equilibrium condensates, in terms of S/Al vs. Si/Al and S/Al vs. Na/Al diagrams, where Al represents a refractory (and relatively immobile) element. The figure shows equilibrium condensate trajectories for a cosmic composition (D/G = 1) as well as a strongly dust-dominant composition (D/G = 10^4) for two different pressures (10^{-6} and 10^{-3} bar).

Variations in S/Al for AO and Type II objects are especially large, spanning three orders of magnitude (Fig. 9a). We attribute this large variation to the mobilization of S during heating. Heating will cause S/Al in condensates to fall dramatically, as S is highly volatile. Type II chondrules, which have low S/Al, could represent partly melted heating residues (condensates) produced by driving S into vapor. Conversely, objects with high S/Al (troilite-rimmed AO objects) could represent objects that reacted with the S-rich gas that was produced by evaporation (Fig. 9a).

Most Type II chondrules and some AO objects (including representatives of all types) form a cluster at low Na/Al (~0.2 at.) and low S/Al (<1 at.) values (the 'Type II cluster') near one possible condensate path (Fig. 9b). These

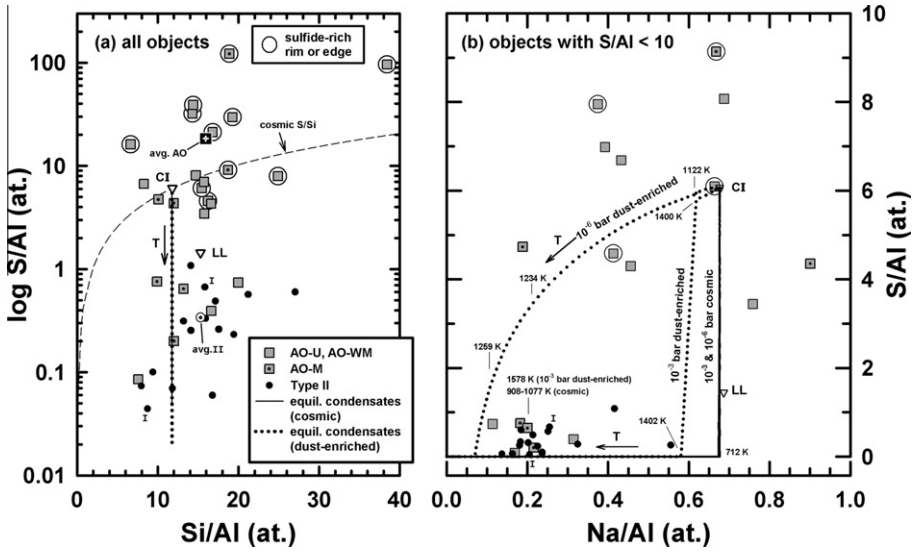

Fig. 9. Bulk compositions of AO objects and Type II chondrules compared to the compositions of equilibrium condensates in systems with overall cosmic (D/G = 1) and dust-enriched (D/G = 10^4) compositions (based on the CWPI thermodynamic code). (a) S/Al vs. Si/Al (all objects) and (b) S/Al vs. Na/Al (objects with S/Al < 10). 'T' with an arrow shows the trend of increasing temperature. 'avg. AO' = mean AO composition, 'avg. II' = mean Type II chondrule composition, 'CI' = mean composition of CI chondrites (Anders and Grevesse, 1989), 'LL' = mean composition of LL chondrites (Jarosewich, 1990), 'I' refers to objects better described as Type I or transitional Types I–II. Note: S/Al scale is logarithmic in part a, and linear in part b.

data are consistent with evaporation of both Na and S to form Type II chondrules and some AO objects.

Sulfur and Na vaporization depends on the heating conditions (Yu et al., 1996). For evaporating systems with cosmic composition, equilibrium models predict loss of S before Na (i.e., S is more volatile than Na), followed by Na loss, with compositions that pass through the Type II cluster (Fig. 9b). For these systems, a heating temperature of ~900–1100 K (depending on pressure) is needed to match the subchondritic S and Na contents of the Type II cluster. However, these temperatures are too low to result in silicate melting and clearly cannot account for the textures of Type II chondrules or melted AO objects.

Systems with very high D/G are more promising for allowing both evaporation and melting. The equilibrium evaporation trajectory will depend on the pressure. With D/G = 10^4 and $P = 10^{-6}$ bar, Na and S are similarly volatile and the evaporation trajectory misses the Type II cluster (Fig. 9b). For the same D/G values and $P = 10^{-3}$ bar, however, S is more volatile than Na and the evaporation trajectory passes through the Type II cluster, with Na/Al ~0.2 attained at a temperature of ~1580 K (Fig. 9b). A similar situation arises for $P = 10^{-3}$ bar at D/G = 10^3 and 10^5, with Na/Al ~0.2 attained at T ~1406 and ~1692 K, respectively. Thus, high pressures (10^{-3} bar) and elevated D/G values can explain the characteristics of the Type II cluster. Moreover, as the solidus for chondrules is estimated to be ~1300–1500 K (Connolly et al., 2006), silicate melt would be expected for systems with elevated D/G values at 10^{-3} bar. This is consistent with the results of Ebel and Grossman (2000), who included a multi-component silicate melt in thermodynamic models and found that such a melt would be stable at $T \geqslant$ 1300–1400 K for D/G values $\geqslant$500–1000 at various pressures (10^{-6}–10^{-3} bar).

We therefore suggest that evaporation to form Type II and melted AO objects occurred at high P (~10^{-3} bar) and D/G values (>500–1000, possibly as high as 10^4–10^5), with an equilibration T of ~1410–1690 K. This T could be either the maximum temperature experienced by the objects, or a closure temperature (specifically, an Na closure temperature) during cooling. The low but non-zero contents of S in the Type II cluster presumably reflect either back-reaction with gas during cooling or incomplete removal of S during heating.

Although variations in S/Al and Na/Al can be largely explained by volatility effects, variations in Si/Al and in other major elements require a different explanation as they show no relationship to the volatile elements (Fig. 9a). The variation in Si/Al is correlated with Mg/Al (Weisberg and Prinz, 1996) but not correlated with Na/Al (Fig. EA-1-2, Electronic Annex), and we suggest that mixing of olivine, pyroxene, and feldspathic material in precursors can explain these data. Specifically, objects that have high Si/Al values are dominated by olivine, and those that have low Si/Al values are dominated by pyroxene and feldspathic glass or feldspar, suggesting that the precursors to AO and Type II objects had variable proportions of these silicates.

Formation of AO and Type II objects under oxidizing conditions is also implied by the ferroan composition of olivine in the objects. Fig. 10 shows Fa contents in olivine for a variety of D/G values at two pressures as obtained with the CWPI code. At temperatures sufficiently high to cause silicate melting (>1300 K), Fig. 10 implies that equilibrium Fa contents resembling those in AO objects and Type II chondrules can be attained only for systems with D/G values of order 10^4–10^5. Using a different thermodynamic code, Ebel and Grossman (2000) found that at

10^{-3} bar pressure, a D/G value of 500 and 1000 would be in equilibrium with olivine with Fa contents as high as ~15 and ~31, respectively, at the solidus ($T \sim 1300$–1400 K). These Fa contents are higher than predicted by the CWPI code for the same conditions, possibly owing to a different thermodynamic treatment of multicomponent melt. Nonetheless, it is apparent that to stabilize ferroan olivine at high temperature, distinctly non-cosmic, high D/G (high gas O/H) values are needed.

One alternative to avoid having high D/G values is to suppose that ferrous olivine compositions were 'inherited' from a pre-existing low-temperature condition which could have produced fayalitic olivine. Inheritance from low T might occur if heating events were too brief to allow equilibration at high T. Fig. 10 shows that Fa > 10 can be obtained at $T < 500$ K for a cosmic system, and at $T < 700$ K for a D/G value of 1000. However, at such low temperatures, diffusion rates are sluggish and it seems dubious that ferroan olivine could form by any process requiring diffusional exchange in olivine (e.g., Fedkin and Grossman, 2005). Another objection to the inheritance model is that olivine grains do not show the zoning that would be expected for such a model. In systems with D/G values $\leqslant 10^3$, olivine becomes more magnesian at higher temperatures (Fig. 10; Ebel and Grossman, 2000), so partial re-equilibration during heating would result in grains with magnesian rims and ferrous cores, unlike what is found in AO objects, which have olivine grains either unzoned or zoned with magnesian cores and ferrous rims. Thus, the ferroan composition of olivine in AO objects probably was not inherited from a low T condition.

AO objects contain fine-grained ferrous grains as well as coarser magnesian relict grains. Heating in these objects would have had to occur in such a way as to equilibrate only the fine grains, and not the coarser grains. In Fig. 11, we evaluate the ability of olivine grains of different sizes (1, 10, and 100 μm in diameter) to equilibrate during *single* chondrule heating events, modeled as ~1 min in duration to peak temperatures of 1600 or 1900 K, with subsequent cooling rates of 100 or 1000 K/h. These heating and cooling conditions are representative of inferences made for chondrules (e.g., Connolly et al., 2006, and references therein), although the 1600 K temperature is considered specifically because it corresponds to a representative closure temperature as discussed above.

Fig. 11 shows that if heating occurred to a typical chondrule peak temperature of 1900 K, grains ranging from several to over 10 μm in diameter (depending on cooling rate) should have equilibrated, whereas larger grains would not have equilibrated. Even if heating occurred to only 1600 K, grains of ~1 μm diameter should have equilibrated if cooling rates were rapid (1000 K/h) and grains a few μm across should have equilibrated if cooling rates were slower (100 K/h) (Fig. 11). Considering that heating events may have been longer than assumed or occurred more than once, diffusion constraints are consistent with fine olivine grains in AO objects (<5–10 μm across) equilibrating at T_{max}. The main conclusion to be drawn is that the fine olivine grains in AO and Type II objects reflect relatively oxidizing conditions during heating.

We do not claim that such oxidizing conditions necessarily pertained to large regions of the nebula. To the contrary, given that most of the gas appears to have been generated by vaporization of dust in dust-enriched regions, it is likely that oxidizing gas was spatially localized and transient. It may have existed only as long as the time needed for chondrule formation.

4.5. Processing of dust to make chondrules

Fig. 12 schematically illustrates our model for how dust was processed in the early solar system. AO objects were

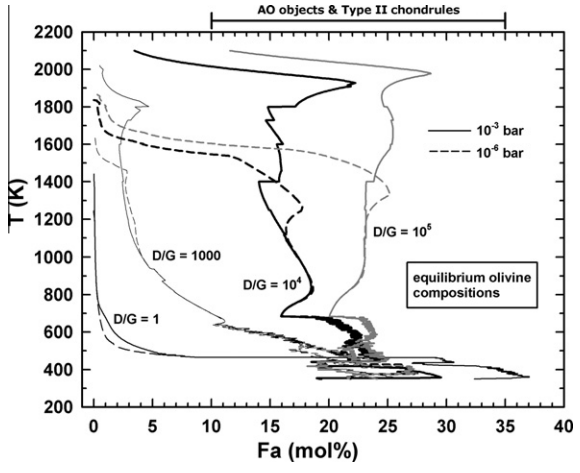

Fig. 10. Equilibrium Fa contents in olivine as a function of temperature for various dust/gas (D/G × cosmic) ratios and pressures, as obtained with the CWPI thermodynamic code.

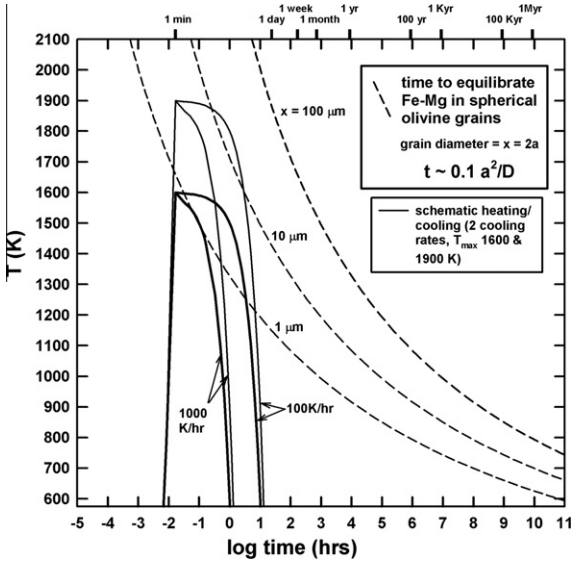

Fig. 11. Time needed to equilibrate Fe-Mg in spherical olivine grains of different diameters (1, 10, 100 μm) (dashed lines) based on the diffusion data of Chakraborty (1997), compared to schematic heating-cooling paths for chondrules which assume a short (~1 min) duration of heating to two peak temperatures (1600 K, 1900 K) and two different cooling rates (100 K/h, 1000 K/h).

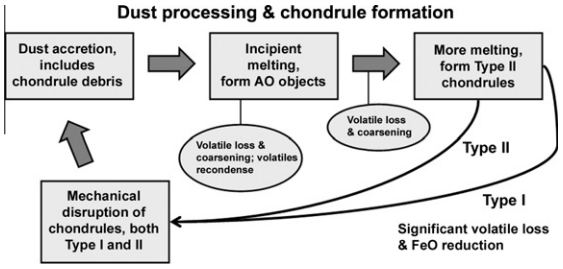

Fig. 12. Model of dust processing and chondrule formation.

formed by dust accretion and subsequent heating, and Type II chondrules were made by progressive heating of AO objects. Heating involved grain coarsening and volatile (S, Na) loss, with volatiles substantially recondensing as AO object dust. An important constituent of the accreted dust for AO objects was chondrule debris, including material derived both from ferroan (Type II) and magnesian (Type I) chondrules. Thus, mechanical disruption of chondrules must have preceded the formation of AO dust clumps. Type II chondrules could have been intensely heated and transformed into Type I chondrules by significant volatile loss and FeO reduction (Huang et al., 1996; Cohen et al., 2004; Ruzicka et al., 2008).

AO material may have played an important role in recycling Type I chondrules into Type II chondrules. Conversion of Type I to Type II chondrules would require the addition of volatiles; one possibility is exchange between gas and Type I chondrules while they were partially molten (Ruzicka et al., 2008). The present work suggests another possibility: volatiles may have been added by the accretion of volatile-rich fine-grained constituents to Type I chondrule fragments to form AO objects, and by subsequent melting of this assemblage to create Type II chondrules. In this case, Type I chondrules are converted to Type II after partial disaggregation and passing through an AO object stage.

The high gas pressures (10^{-3} bar) inferred for ferroan AO objects and Type II chondrules are plausible for the nebula, if much gas was locally derived by the evaporation of dust. However, the Type II and AO objects we studied show clearly that evaporation effects were limited only to the most volatile elements, not to major elements such as Mg and Si (Section 4.4). Thus, one needs to invoke substantially more heating and attendant vaporization of dust elsewhere in the system to create the high pressure gas. Dust processing and chondrule formation therefore must have occurred in such a way as to allow variable particle heating in the same general location of the nebula, ranging from vaporization, to melting, to annealing.

4.6. Chondrule formation by nebular shock waves?

The nebular shock wave model has emerged as the favored and best-constrained mechanism for forming chondrules (e.g., Hood and Horányi, 1991, 1993; Boss, 1996, 2005; Connolly and Love, 1998; Jones et al., 2000; Iida et al., 2001; Desch and Connolly, 2002; Miura et al., 2002; Ciesla, 2005; Desch et al., 2005; Connolly et al., 2006; Miura and Nakamoto, 2005). This model is compatible with our observations, as explained below.

(1) *Heating by nebular shock waves can explain the transformation of unmelted fine dust into coarser melted objects.* With this mechanism grains less <10 μm across are predicted either to not melt (for slow-moving shocks) or to vaporize (for fast-moving shocks), unlike coarser particles that melt (Miura and Nakamoto, 2005). This implies that fine-grained AO material (<10 μm across) prior to its agglomeration into inclusions or rims could have been annealed, or that it could have condensed from vaporized gas, but that it would not have melted. However, once the dust accreted to form an agglomerate (AO object), it could have melted. This agrees with our observations.

(2) *The shock wave model can explain accretionary structures.* As particles of different sizes will accelerate differently in shocked gas, one can expect the accretion of fine-grained material onto coarser objects, as the latter run into the former (Connolly and Love, 1998). The fine-grained material would be less heated, so objects with coarse-grained cores surrounded by fine-grained (AO-like) rims could be explained.

(3) *Nebular shock waves can explain a high pressure nebular formation environment.* Transient high pressures of $\sim 10^{-3}$ bar can be generated during passage of a shock wave, or up to two orders of magnitude higher pressure than canonical ambient nebular gas (Connolly and Love, 1998; Desch and Connolly, 2002). A high pressure origin matches the conditions of evaporative melting proposed here (Section 4.5), and makes chemical-isotopic exchange between chondrule liquids and surrounding gas likely (Miura et al., 2002). Such back-reaction is suggested to account for textures and the Na and S contents in AO objects and chondrules. However, a two orders of magnitude increase in pressure implies a maximum D/G value of 100, which is too low for ferroan chondrules. A larger increase in pressure and a larger D/G is needed.

(4) *The shock wave model can explain variable heating effects occurring in proximal materials.* Our data suggest that the chondrule-forming mechanism must have allowed variable heating of different constituents, with these constituents sufficiently proximal to allow interactions between annealed, melted, and vaporized material (Section 4.5). Differential heating by particle size is one aspect of shock wave heating consistent with the observations.

(5) *Complementary chemical and textural features between chondrules and AO objects for some elements are consistent with the variable heating of chondritic dust.* Previous researchers have noted an apparent chemical relationship between chondrules and matrix or matrix-like rims and suggested that heating could have driven volatiles from chondrule precursors into a gas phase, which condensed as fine, matrix-like

particles (e.g., Kong et al., 1999; Kong and Palme, 1999; Bland et al., 2005; Hezel and Palme, 2010). Metal may have been expelled from chondrules and mixed with fine-grained dust (Grossman and Wasson, 1987; Lauretta and Buseck, 2003; Bland et al., 2005). Our data are consistent with the partial removal of S, Fe, and Ni from chondrules and their incorporation into AO object dust, and with the partial removal of Na from AO object dust during heating to make chondrules.

(6) *The shock wave model can explain the presence of apparent chondrule fragments in AO objects.* Fragmentation of objects potentially can occur in shock waves (Connolly and Love, 1998) and ram pressure might also limit the ability of larger melt drops to form (Susa and Nakamoto, 2002). Thus, the same process potentially can produce both chondrule debris within, and the heating of, AO objects.

5. CONCLUSION

(1) AO objects in ordinary chondrites formed by the accretion of dust followed by variable heating. AO object dust included chondrule debris and on average had a composition similar to whole-rock ordinary chondrites. Some objects were largely sintered, others were partly melted.

(2) There is good evidence that ferroan AO objects are protochondrules, and that they were melted to form Type II chondrules.

(3) Progressive heating during chondrule formation resulted in grain coarsening and evaporative melting. Coarsening occurred by crystallization from incomplete melts. Sulfur, Na, and a Fe + Ni (metal) component were partly lost during heating.

(4) In AO objects, troilite formed by crystallization from a melt, mostly likely in the form of a metallic melt condensate.

(5) The ferroan compositions of fine-grained olivine in AO objects reflect oxidizing conditions during heating, and the bulk compositions and textures of Type II chondrules imply that heating occurred at relatively high pressures ($\sim 10^{-3}$ bar) in an oxidizing gas. These oxidizing, high pressure conditions probably reflect transient conditions created by the evaporation of dust in regions with dust/gas ratios >500–1000 and possibly up to 10^4–$10^5 \times$ cosmic. The fine-grained fraction of Type II chondrules approached equilibration at a temperature of ~1410–1690 K.

(6) Fine-grained matrix-like materials in chondrites did not all form in the same way; two matrix lumps had a different origin than AO objects.

(7) The trace-element bulk compositions of fine-grained materials in AO objects and Type II chondrules are sensitive recorders of melting and metamorphic processes. Metamorphism in subtype 3.5 materials resulted in the formation of phosphate that caused local elemental re-distribution.

(8) The data are compatible with the nebular shock wave model for chondrule formation.

ACKNOWLEDGMENTS

This work was supported by NASA grant NNG06GE17G (A.R.). We thank Dominik Hezel, Derek Sears, and Harold Connolly for helpful reviews that improved the quality of this manuscript, and Hiroko Nagahara for editorial handling.

APPENDIX A. DETAILS ON EXPERIMENTAL CONDITIONS AND METHODS

Electron microprobe: Major and minor elements were analyzed using an electron microprobe at Oregon State University in wavelength-dispersive mode. Operating conditions included a 15 KeV accelerating voltage and a beam current of 50 nA. Well-characterized minerals and glasses were used as standards, and data were reduced using the nominal Cameca PAP procedure (Pouchou and Pichoir, 1985). Nominal criteria for accepting analyses included totals between 97 and 102 wt%; cations/4O for olivine ranging from 2.95 to 3.05 (most analyses had 2.98–3.02); and cations/6O for pyroxene ranging from 3.93 to 4.07 (most analyses had 4.00–4.03).

Norm calculation: 'Defocused' beam EMPA data (DB-EMPA) were obtained to estimate mineral proportions in analysis areas using a norm calculation. The calculation assumes as possible normative minerals the phases that are found in AO objects. These include: olivine, low-Ca pyroxene or orthopyroxene (the sum of normative enstatite + ferrosilite), clinopyroxene (diopside + hedenbergite), plagioclase (albite + anorthite), metal [with assumed 28 wt% Ni, equivalent to the average composition of metal in LL chondrites (Jarosewich, 1990)], chromite, and troilite. All chlorine was assumed to be present in the form of sodalite, but the actual siting of Cl was not determined in most cases. All Fe remaining after assignment to troilite and metal was partitioned in olivine and pyroxene according to apparent Mg#. The following mineral densities (ρ, all in g/cm^3 and based on Gaines et al., 1997) were assumed to convert weight to volume fractions for mineral phases: $\rho_{\text{forsterite}} = 3.24$, $\rho_{\text{fayalite}} = 4.39$, $\rho_{\text{diopside}} = 3.28$, $\rho_{\text{hedenbergite}} = 3.65$, $\rho_{\text{enstatite}} = 3.20$, $\rho_{\text{ferrosilite}} = 4.00$, $\rho_{\text{anorthite}} = 2.76$, $\rho_{\text{albite}} = 2.62$, $\rho_{\text{Fe-metal}} = 7.97$, $\rho_{\text{Ni-metal}} = 8.14$, $\rho_{\text{chromite}} = 5.06$, $\rho_{\text{sodalite}} = 2.30$, $\rho_{\text{troilite}} = 4.84$.

Corrected DB-EMPA data: Apparent initial mineral proportions implied by the norm were used together with measured or assumed phase compositions and mineral densities to estimate correction factors based on the unequal-density effect (Warren, 1997). The effect of the correction is to adjust the wt% concentration of elements sited in high-density phases (e.g., Fe in metal and troilite) upwards and the concentration of elements sited in low-density phases (e.g., Na and Al in feldspar) downwards. The

corrected ('true') norm was then recalculated for each analysis.

Ion microprobe: SIMS was used to analyze trace elements at Washington University. All analyses were made using an O^- primary beam and energy filtering at low mass resolution to remove complex molecular interferences. The resulting mass spectrum was deconvolved in the mass ranges K–Ca–Sc–Ti and Rb–Sr–Y–Zr to remove simple molecular interferences that are not eliminated with energy filtering (Alexander, 1994; Hsu, 1995). Sensitivity factors for the REE are from Zinner and Crozaz (1986b), and those for other elements are from Hsu (1995) and are listed in Table 1 of Floss et al. (1998). For mixed phases, average sensitivity factors are used for Mg, Fe and Ca, and average (non-plagioclase) sensitivity factors are assumed for the REE. Absolute concentrations were determined by normalizing ion signal concentrations to concentrations determined by electron microprobe analysis, using Si as the normalizing element. Each SIMS analysis was evaluated to take into account the possibility of analyzing off the desired target area. Apparent concentrations derived by SIMS were compared to concentrations obtained by EMPA for the same elements at the same or nearby location. If values agreed substantially, the analysis was accepted as is. If the values did not substantially agree, the analysis was rejected.

Thermodynamic modeling: For comparison to AO data, we used a version of the CWPI thermodynamic code (Petaev and Wood, 1998, 2005), developed and kindly provided by Mikhail Petaev, to model condensate compositions in a 20-element system (H, He, C, N, O, Na, Mg, Al, Si, P, S, Cl, K, Ca, Ti, Cr, Mn, Fe, Co, Ni). For all runs, isobaric conditions and complete equilibrium (no isolation of condensates) were assumed so as to minimize the number of free parameters. Investigated system compositions included 'cosmic', based on the average composition of CI chondrites (Anders and Grevesse, 1989), and 'dust-enriched' systems (e.g., Wood and Hashimoto, 1993; Ebel and Grossman, 2000). In runs of given pressure and system composition, temperature was varied in 2 K intervals.

APPENDIX B. SUPPLEMENTARY DATA

Supplementary data (Electronic Annex 1 file) associated with this article can be found, in the online version, at doi:10.1016/j.gca.2011.10.020.

REFERENCES

Alexander C. M. O'D. (1994) Trace element distributions within ordinary chondrite chondrules: implications for chondrule formation conditions and precursors. *Geochim. Cosmochim. Acta* **58**, 3451–3467.

Allen J. S., Nozette S. and Wilkening L. L. (1980) A study of chondrule rims and chondrule irradiation records in unequilibrated ordinary chondrites. *Geochim. Cosmochim. Acta* **44**, 1161–1175.

Anders E. and Grevesse N. (1989) Abundances of the elements: meteoritic and solar. *Geochim. Cosmochim. Acta* **53**(1989), 197–214.

Ashworth J. R. (1977) Matrix textures in unequilibrated oridinary chondrites. *Earth Planet. Sci. Lett.* **35**, 25–34.

Bland P. A., Alard O., Benedix G. K., Kearsley A. T., Menzie O. N., Watt L. E. and Rogers N. W. (2005) Volatile fractionation in the early solar system and chondrule/matrix complementarity. *Proc. Natl. Acad. Sci.* **102**, 13755–13760.

Boss A. P. (1996) A concise guide to chondrule formation. In *Chondrules and the Protoplanetary Disk* (eds. R. Jones and E. Scott). Cambridge University Press, Cambridge, pp. 257–263.

Boss A. P. (2005) The solar nebula. In *Meteorites, comets, and planets* (ed. A. M. Davis). Treatise on Geochemistry, vol. 1, Elsevier, Amsterdam. pp. 63–82.

Chakraborty S. (1997) Rates and mechanisms of Fe–Mg interdiffusion in olivine at 980 °C–1300 °C. *J. Geophys. Res.* **102**, 12317–12331.

Ciesla F. J. (2005) Chondrule-forming processes – An overview. In *Chondrites and the Protoplanetary Disk* (eds. A. N. Krot, E. R. D. Scott, B. Reipurth). ASP Conference Series v. 341. pp. 811–820.

Cohen B. A., Hewins R. H. and O'D Alexander. C. M. (2004) The formation of chondrules by open-system melting of nebular condensates. *Geochim. Cosmochim. Acta* **68**, 1661–1675.

Connolly, Jr., H. C. and Love S. G. (1998) The formation of chondrules: petrologic tests of the shock wave model. *Science* **280**, 62–67.

Connolly, Jr., H. C., Desch S. J., Ash R. D. and Jones R. H. (2006) Transient heating events in the protoplanetary nebula. In *Meteorites and the Early Solar System II* (eds. D. S. Lauretta and H. Y. McSween). University of Arizona Press, Tucson, pp. 383–397.

Desch S. J. and Connolly, Jr., H. C. (2002) A model for the thermal processing of particles in the solar nebula shocks: application to cooling rates of chondrules. *Meteorit. Planet. Sci.* **37**, 183–208.

Desch S. J., Ciesla F. J., Hood L. L. and Nakamoto T. (2005) Heating of chondritic materials in solar nebula shocks. In *Chondrites and the Protoplanetary Disk* (eds. A. N. Krot, E. R. D. Scott, B. Reipurth). ASP Conference Series v. 341. pp. 849–872.

Dodd R. T. and Van Schmus W. R. (1971) Dark-zoned chondrules. *Chem. Erde* **30**, 49–69.

Ebel D. S. and Grossman L. (2000) Condensation in dust-enriched systems. *Geochim. Cosmochim. Acta* **64**, 339–366.

Fedkin A. V. and Grossman L. (2005) The fayalite content of chondritic olivine: obstacle to understanding the condensation of rocky material. In *Meteorites and the Early Solar System II* (eds. D. S. Lauretta and H. Y. McSween). University of Arizona Press, Tucson, pp. 279–294.

Floss C., James O. B., McGee J. J. and Crozaz G. (1998) Lunar ferroan anorthosite petrogenesis: clues from trace element distributions in FAN subgroups. *Geochim. Cosmochim. Acta* **62**, 1255–1283.

Fujimaki (1986) Partition coefficients of Hf, Zr, and REE between zircon, apatite, and liquid. *Contrib. Mineral. Petrol.* **94**, 42–45.

Gaines R. V., Skinner H. C. W., Foord E. E., Mason B. and Rosenzweig A. (1997) *Dana's New Mineralogy—The System of Mineralogy of James Dwight Dana and Edward Salisbury Dana*, 8th Ed. John Wiley & Sons Inc., New York, pp. 1819.

Grossman J. N. (1999) The Meteoritical Bulletin No. 83, 1999 July. *Meteorit. Planet. Sci.* **34**, A169–A186.

Grossman J. N. and Wasson J. T. (1987) Compositional evidence regarding the origins of rims on Semarkona chondrules. *Geochim. Cosmochim. Acta* **51**, 3003–3011.

Hewins R. H. (1997) Chondrules. *Annu. Rev. Earth Planet. Sci.* **25**, 61–83.

Hewins R. H. and Fox G. E. (2004) Chondrule texture and precursor grain size: an experimental study. *Geochim. Cosmochim. Acta* **68**, 917–926.

Hewins R. H., Zanda B. and Bourot-Denise M. (1996) Evaporative loss and degree of melting in Semarkona type I chondrules. *Lunar Planet Sci.* **27**, 537–538.

Hewins R. H., Yu Y., Zanda B. and Bourot-Denise M. (1997) Do nebular fractionations, evaporative losses, or both, influence chondrule compositions? *Antarct. Meteorite Res.* **10**, 275–298.

Hezel D. C. and Palme H. (2010) The chemical relationship between chondrules and matrix and the chondrule–matrix complementarity. *Earth Planet. Sci. Lett.* **294**, 85–93.

Hood L. L. and Horányi M. (1991) Gas dynamic heating of chondrule precursor grains in the solar nebula. *Icarus* **93**, 259–269.

Hood L. L. and Horányi M. (1993) The nebula shock wave model for chondrule formation: one-dimensional calculations. *Icarus* **106**, 179–189.

Hsu W. (1995) Ion microprobe studies of the petrogenesis of enstatite chondrites and eucrites. Ph. D. thesis, Washington University.

Huang S., Lu J., Prinz M., Weisberg M. K., Benoit P. H. and Sears D. W. G. (1996) Chondrules: their diversity and the role of open-system processes during their formation. *Icarus* **122**, 316–346.

Iida A., Nakamoto T., Susa H. and Nagasawa Y. (2001) A shock heating model for chondrule formation in a protoplanetary disk. *Icarus* **153**, 430–450.

Jarosewich E. (1990) Chemical analyses of meteorites: a compilation of stony and iron meteorite analyses. *Meteoritics* **25**, 323–337.

Jones R. H., Lee T., Connolly, Jr., H. C., Love S. G. and Shang H. (2000) Formation of chondrules and CAIs: theory vs. observation. In *Protostars and Planets IV* (eds. V. Manning, A. P. Boss and S. S. Russell). University of Arizona, Tucson, pp. 927–962.

Kallemeyn G. W., Rubin A. E., Wang D. and Wasson J. T. (1989) Ordinary chondrites: bulk compositions, classification, lithophile-element fractionation, and composition-petrographic type relationships. *Geochim. Cosmochim. Acta* **53**, 2747–2767.

Kennedy A. K., Lofgren G. E. and Wasserburg G. J. (1993) An experimental study of trace element partitioning between olivine, orthopyroxene and melt in chondrules: equilibrium values and kinetic effects. *Earth Planet. Sci. Lett.* **115**, 177–195.

King T. V. V. and King E. A. (1981) Accretionary dark rims in unequilibrated chondrites. *Icarus* **48**, 460–472.

Kojima T., Lauretta D. S. and Buseck P. R. (2003) Accretion, dispersal, and reaccumulation of the Bishunpur LL3.1 brecciated chondrite: evidence from troilite-silicate-metal inclusions and chondrule rims. *Geochim. Cosmochim. Acta* **67**, 3065–3078.

Kong P. and Palme H. (1999) Compositional and genetic relationship between chondrules, chondrule rims, metal, and matrix in the Renazzo chondrite. *Geochim. Cosmochim. Acta* **63**, 3673–3682.

Kong P., Ebihara M. and Palme H. (1999) Distribution of siderophile elements in CR chondrites: evidence for evaporation and recondensation during chondrule formation. *Geochim. Cosmochim. Acta* **63**, 2637–2652.

Krot A. N. and Wasson J. T. (1995) Igneous rims on low-FeO and high-FeO chondrules in ordinary chondrites. *Geochim. Cosmochim. Acta* **59**, 4951–4966.

Lauretta D. S. and Buseck P. R. (2003) Opaque minerals in chondrules and fine-grained chondrule rims in the Bishunpur (L3.1) chondrite. *Meteorit. Planet. Sci.* **38**, 59–79.

Lodders K. (2003) Solar system abundances and condensation temperatures of the elements. *Astrophys. J.* **591**, 1220–1247.

Lodders K. and Fegley, Jr., B. (1998) *The Planetary Scientist's Companion*. Oxford University Press, New York, pp. 371.

Metzler K. and Bischoff A. (1996) Constraints on chondrite agglomeration from fine-grained chondrule rims. In *Chondrules and the Protoplanetary Disk* (eds. R. Hewins, R. Jones and E. Scott). Cambridge University Press, Cambridge, pp. 153–161.

Metzler K., Bischoff A. and Stöffler D. (1992) Accretionary dust mantles in CM chondrites: evidence for solar nebula processes. *Geochim. Cosmochim. Acta* **56**, 2873–2897.

Miura H. and Nakamoto T. (2005) A shock-wave heating model for chondrule formation II. Minimum size of chondrule precursors. *Icarus* **175**, 289–304.

Miura H., Nakamoto T. and Susa H. (2002) A shock-wave heating model for chondrule formation: effects of evaporation and gas flows on silicate particles. *Icarus* **160**, 258–270.

Nazarov M. A., Ignatenko K. I. and Shevaleevsky I. D. (1982) Source of errors in defocussed beam analysis with the electron probe, revisited. *Lunar Planet. Sci. XIII*, 582–583.

Okazaki R. and Nakamura T. (2005) Origin and thermal history of lithic materials in the Begaa LL3 chondrite. *Lunar Planet. Sci. XXXVI*. Abstract #1533.

Petaev M. I. and Wood J. A. (1998) The condensation and partial isolation (CWPI) model of condensation in the solar nebula. *Meteorit. Planet. Sci.* **33**, 1123–1137.

Petaev M. I. and Wood J. A. (2005) Meteoritic constraints on temperatures, pressures, cooling rates, chemical compositions, and modes of condensation in the solar nebula. In *Chondrites and the Protoplanetary Disk* (eds. A. N. Krot, E. R. D. Scott, B. Reipurth). ASP Conference Series v. 341. pp. 373–406.

Pouchou J. L. and Pichoir F. (1985) "PAP" procedure for improved quantitative microanalysis. In *Microbeam Analysis* (ed. J. T. Armstrong). San Francisco Press, Inc., San Francisco, pp. 104–106.

Rubin A. E. (1984) Coarse-grained chondrule rims in type 3 chondrites. *Geochim. Cosmochim. Acta* **48**, 1779–1789.

Russell S. S., Zolensky M., Righter K., Folco L., Jones R., Connolly, Jr., H. C., Grady M. and Grossman J. N. (2005) The Meteoritical Bulletin No. 89, 2005 September. *Meteorit. Planet. Sci.* **40**, A201–A263.

Ruzicka A., Floss C. and Hutson M. (2008) Relict olivine grains, chondrule recycling, and implications for the chemical, thermal, and mechanical processing of nebular materials. *Geochim. Cosmochim. Acta* **72**, 5530–5557.

Ruzicka A., Floss C. and Hutson M. (2010) Accretion and melting of dust to form ferroan chondrules in ordinary chondrites. *Lunar Planet. Sci. XXXXI*, Abstract #1956. Lunar and Planetary Institute.

Ruzicka A. and Hutson M. (2011) Agglomeratic olivine (AO) objects: melting of dust to create Type II chondrules. *Workshop on Formation of the First Solids of the Solar System*. Abstract #9020.

Sears D. W. G., Lu J., Benoit P. H., DeHart D. M. and Lofgren G. E. (1992) A compositional classification scheme for meteoritic chondrules. *Nature* **357**, 207–211.

Sears D. W. G., Shaoxiong H. and Benoit P. H. (1995) Chondrule formation, metamorphism, brecciation, an important new primary chondrule group, and the classification of chondrules. *Earth Planet. Sci. Lett.* **131**, 27–39.

Susa H. and Nakamoto T. (2002) On the maximal size of chondrules in shock wave heating model. *Astrophys. J.* **564**, L57–L60.

Van Schmus W. R. (1969) The mineralogy and petrology of chondritic meteorites. *Earth Sci. Rev.* **5**, 145–184.

Warren P. H. (1997) The unequal host-phase density effect in electron probe defocused beam analysis: an easily correctable problem. *Lunar Planet. Sci. XXVIII*. Abstract #1406.

Watson E. B. and Green T. H. (1981) Apatite/liquid partition coefficients for the rare Earth elements and strontium. *Earth Planet. Sci. Lett.* **56**, 405–421.

Weisberg M. K. and Prinz M. (1994) Agglomeratic olivine (AO) chondrules in ordinary chondrites. *Lunar Planet. Sci. XXV*, 1481–1482.

Weisberg M. K. and Prinz M. (1996) Agglomeratic chondrules, chondrule precursors, and incomplete melting. In *Chondrules and the Protoplanetary Disk* (eds. R. Hewins, R. Jones and E. Scott). Cambridge University Press, Cambridge, pp. 119–127.

Weisberg M. K., Smith C., Benedix G., Herd C. D. K., Righter K., Haack H., Yamaguchi A., Chennaoui Aoudjehane H. and Grossman J. N. (2009) The Meteoritical Bulletin No. 96, September 2009. *Meteorit. Planet. Sci.* **44**, 1355–1357.

Wood J. A. and Hashimoto A. (1993) Mineral equilibrium in fractionated nebular systems. *Geochim. Cosmochim. Acta* **57**, 2377–2388.

Yu Y., Hewins R. H. and Zanda B. (1996) Sodium and sulfur in chondrules: heating and cooling curves. In *Chondrules and the Protoplanetary Disk* (eds. R. Hewins, R. Jones and E. Scott). Cambridge University Press, Cambridge, pp. 213–219.

Zinner E. and Crozaz G. (1986a) A method for the quantitative measurement of rare earth elements by ion microprobe. *Int. J. Mass Spectrom. Ion Processes* **69**, 17–38.

Zinner E. and Crozaz G. (1986b) Ion probe determination of the abundances of all the rare earth elements in single mineral grains. In *Secondary Ion Mass Spectrometry, SIMS V* (eds. A. Benninghoven, R. J. Colton, D. S. Simons and H. W. Werner). Springer-Verlag, New York, pp. 444–446.

Associate editor: Hiroko Nagahara

Electronic Annex for GCA manuscript, *"Agglomeratic olivine (AO) objects and Type II chondrules in ordinary chondrites: Accretion and melting of dust to form ferroan chondrules"*

By Alex Ruzicka, Christine Floss, Melinda Hutson

Contents:

Electronic Annex EA-1
Petrographic and bulk-chemical (EMPA) data

Table EA-1-1. Petrographic and olivine chemical data for the 32 objects included in this study.

Object	Overall size[1] (mm)	Core texture & mineralogy[2]	Rim texture & mineralogy[2]	Olivine grain size[2] (μm)	Olivine composition[2]
Beg-1	0.8-1	Type II PO, gl, troi, relict Mg-px	Fine-gr Fe-ol, gl, relict Mg-px & chondrule, massive troi	10-250 core, < 5 rim	Fo_{82-91}
Beg-2	0.70-0.75	Fine-gr Fe-ol, troi, gl?, relict Mg-ol & chondrules	Partial troi-rich edge	<5	Fo_{75-81} normal, Fo_{97} relict
Beg-3	0.45-0.70	Fine-gr lacy troi, Fe-ol, relict Mg-px & Mg-ol & chondrules	Troi-rich edge	<5	Fo_{69-74} normal, Fo_{95} relict
Beg-4	0.45-0.50	Type II PO, ol, gl, troi, relict Mg-ol	Inner: Fine-gr Fe-ol, gl, troi Outer: Fine-gr Fe-ol, troi	3-80 core, <10 inner rim <5 outer rim	Fo_{75-85} normal, Fo_{98} relict
Beg-5	0.3-0.5	Type II PO, gl, relict Mg-ol & Mg-px	Troi-rich edge	10-100	Fo_{69-85} normal, Fo_{99} relict
Beg-6	1.2-1.4	Fine-gr Type II, gl, relict Mg-ol	Inner: Fine-gr Fe-ol, troi, relict chondrules & Mg-ol. Outer: Lacy troi, Fe-ol, Mg-ol	5-20 core, <5 rim	Fo_{74-85} normal, Fo_{90-91} relict
Beg-7	0.45	Fine-gr Fe-ol, troi, gl?, relict Mg-px & Mg-ol & chondrule	Troi-rich edge	<5	Fo_{65-73} normal, Fo_{99} relict
Beg-8	0.85	Fine-gr Fe-ol, troi, gl, relict chondrules & Mg-ol & Mg-px	Massive troi-rich edge	<10	Fo_{83-88} normal, Fo_{93-95} relict
Beg-10	0.3-0.5	Fine-gr GP, gl, relict Fe-ol & Mg-px	Massive troi-rich edge	<10	Fo_{80-85} (relict)
Beg-11	0.4-0.7	Composite Type II PO & Type I GP (both gl)	Rim absent	10-150	Fo_{70-90} (PO)
Beg-12	0.4-0.8	Ultrafine-gr matrix lump	Rim absent	<1	n.a.
Beg-13	0.45	Fine-gr Type I PO, gl, troi	Fine-gr Fe-ol, troi, Fe-px	<20 core, <5 rim	Fo_{94-96} core, Fo_{72-85} rim
Beg-14	0.32-0.50	Fine-gr Type II PO, gl	Fine-gr Fe-ol, troi	<25 core, <5 rim	Fo_{71-75}
Beg-15	0.90-0.95	Type II PO, many relict ol grains, gl	Rim absent	10-200	Fo_{79-88} normal, Fo_{89-92} relict
Beg-16	0.50-0.65	Type II PO, coarse ol relict, gl	Inner: Fine-gr Fe-ol, gl, troi Outer: Fine-gr Fe-ol, troi	10-80 core (370 relict) <5 rim	n.a.
Beg-16A	0.4-0.5	Fine-gr Fe-ol, troi, relict Mg-px & Mg-ol	Troi-rich edge	<5	Fo_{70-75} normal, Fo_{92} relict
Beg-17	2.5-3.0	Fine-gr Fe-ol, gl, relict Mg-ol & chondrules & Mg-px, troi, met	Fine-gr lacy troi, Fe-ol, Mg-ol	<10	Fo_{83-87} normal, Fo_{88-99} relict

Continued, next page.

Table EA-1-1, concluded.

Object	Overall size[1] (mm)	Core texture & mineralogy[2]	Rim texture & mineralogy[2]	Olivine grain size[2] (μm)	Olivine composition[2]
Beg-17A	0.40-0.45	Ultrafine-gr matrix lump	Rim absent	<2	n.a.
Beg-17X	0.65-0.80	Type II PO, gl, relict Mg-ol	Fine-gr Fe-ol to troi-rich	25-50 core (270 relict) < 5 rim	n.a.
Beg-18A	0.4-0.9	Fine-gr Type II PO, gl, relict Mg-ol & chondrule	Rim absent	5-50	Fo_{71-81} normal, Fo_{83-99} relict
NWA-6	0.8-2.0	Igneous-textured lumps/clasts, altered matrix?	Rim absent	10-250	Fo_{78-98}, not correlated with grain size
NWA-11	2.0	Type II PO, gl	Inner: fine-gr Fe-ol, gl, relict chondrule & Mg-ol, massive troi edge. Outer: ultrafine silicate	10-300 core, 10-15 inner rim, <2 outer rim	Fo_{75-89} core, not correlated with grain size
NWA-11A	0.5	Fine-gr Type II PO, gl	Inner: fine-gr Fe-ol, px. Outer: Fe-ol, Mg-ol & Mg-px relicts, lacy troi, no gl	5-60 core, <5 rim	Fo_{67-84} core & larger rim grains
NWA-11C	0.4	Fo clast	Fine-gr Fe-ol, troi, gl patches inwards	200 clast, <5 rim	$Fo_{99.3-99.4}$ clast
NWA-15	1.0-1.5	Type II PO, devitrified meso, pheno-poor edge, relict Mg-ol	Fine-gr Fe-ol, troi, relict Mg-ol & relict chondrules	10-100 core, <10 rim	Fo_{74-83} normal, Fo_{87-94} relicts
NWA-21	0.6-0.7	Fine-gr Type II PO, gl, relict Mg-ol	Gl-poor, ol-rich	10-50	Fo_{73-88} normal, Fo_{96-99} relicts
Sah98-3	0.26-0.32	Fine-gr Type II, devitrified meso, feldspathoid, relict Mg-ol	Fine-gr Fe-ol, troi	<10 core, <5 rim	Fo_{62-75} normal, Fo_{90-98} relict
Sah98-3A	0.16-0.20	Fine-gr Mg-px, Fe-ol, troi, gl?	Fine-gr Fe-ol, troi, gl?	<5-10 core, <5 rim	Fo_{65-75} rim
Sah98-4B	0.20-0.28	Fine-gr Mg-px, zoned ol, gl	Fine-gr Fe-ol, troi, Mg-px, rare gl	<20 core, <5 rim	Fo_{50-65} rim
Sah98-5	0.80	Fine-gr Type II PO, gl, devitrified meso, relict Mg-px	Rim absent	5-50	Fo_{70-71}
Sah98-12	0.32	Fine-gr GO, px, gl?, troi	Fine-gr Fe-ol, troi, gl?	<5-10 core, <5 rim	Fo_{67-69}
Sah98-13	1.3	Composite IIA PO & I-IIAB POP, intervening I-IIAB	Fine-gr Fe-ol, px, relict Mg-ol & Mg-px, lacy troi-rich edge, minor gl?	10-200 core, <10 rim	Fo_{67-72} core

[1] Approximate diameter in thin section. [2] Predominant texture, mineralogy, olivine composition, and grain size diameter in core (central) and rim (edge) facies of objects. Textures: PO = microporphyritic olivine; GO = granular olivine; GP = granular pyroxene; POP = microporphyritic olivine-pyroxene. Mineralogy: fo = forsterite; ol = olivine; troi = troilite; px = pyroxene (mainly low-Ca); gl = glass, meso = mesostasis. Grain types: normal = grains with typical composition in object; relict = grains with atypically magnesian compositions in object; fine-gr = fine-grained; n.a. = not analyzed

Table EA-1-2. Bulk chemical and normative compositions of objects based on corrected defocused beam microprobe data.*

Object	Beg-1 core	Beg-2	Beg-3	Beg-4 core	Beg-4 rim	Beg-5	Beg-6 core	Beg-6 inner rim	Beg-6 outer rim	Beg-7 interior	Beg-7 edge	Beg-8 interior	Beg-8 edge	Beg-12	Beg-13 core	Beg-13 rim	Beg-14 core
type	coarse IIA	AO-WM	AO-U, troi-rich	coarse IIA	AO-WM troi-rich	coarse IIA	fine IIAB	AO-U	AO-U, troi-rich	AO-WM, troi-rich	AO-WM, troi-rich edge	AO-M, troi-rich	AO-M, troi-rich armor	matrix lump	fine IA	AO-WM, troi-rich	fine IIA / IIAB
N	6	13	18	10	5	5	7	8	5	11	3	13	4	11	2	6	7
Mg# (at.)	0.84	0.74	0.76	0.82	0.69	0.74	0.74	0.68	0.80	0.76	0.80	0.80	0.73	0.69	0.81	0.78	0.70
Wt%																	
SiO_2	39.2	35.0	26.1	32.1	29.8	35.5	39.6	27.8	20.1	28.2	15.9	33.1	7.88	36.6	35.0	21.4	36.5
Al_2O_3	1.23	2.00	2.68	0.22	1.35	0.10	2.38	1.42	0.88	1.62	0.94	2.35	0.35	1.64	0.86	1.08	1.76
Cr_2O_3	0.60	0.76	0.72	0.47	0.78	0.27	1.18	0.77	0.53	0.62	0.89	0.69	0.37	0.90	0.30	0.15	0.74
FeO	15.6	16.7	10.5	14.6	17.8	21.8	16.0	21.4	8.08	13.9	5.49	12.2	4.05	23.0	15.7	11.7	21.2
MnO	0.38	0.30	0.21	0.26	0.24	0.38	0.36	0.3	0.21	0.27	0.23	0.33	0.12	0.96	0.22	0.22	0.40
MgO	38.2	24.1	16.0	35.8	16.0	35.6	24.6	21.1	16.3	18.7	10.4	22.2	5.93	28.6	36.1	17.9	27.9
CaO	0.37	1.65	2.07	0.31	3.72	0.23	2.23	1.33	0.88	2.18	1.05	1.93	0.73	0.43	0.28	0.29	1.38
Na_2O	0.14	0.91	0.7	0.03	0.55	0.02	0.60	0.39	0.35	0.68	0.52	1.28	0.16	0.29	0.17	0.43	0.60
Ni	0.20	1.28	2.35	0.89	0.58	0.18	0.90	2.79	2.57	2.52	3.55	2.12	1.34	0.02	1.23	1.25	0.41
S	0.46	3.97	11.3	3.03	7.75	0.02	1.62	3.84	16.5	8.24	19.0	6.42	27.2	0.11	1.25	14.5	0.29
Cl	<0.01	<0.01	<0.01	0.03	<0.01	0.06	<0.01	<0.01	<0.01	<0.01	<0.01	<0.01	<0.01	<0.01	0.03	0.01	0.01
Fe (troi)	0.81	6.91	19.6	5.27	13.5	0.03	2.82	6.69	28.7	14.4	33.2	11.2	47.4	0.19	2.18	24.3	0.50
Fe (met)	0.49	3.17	5.71	2.15	1.45	0.46	2.24	6.17	4.39	5.91	8.82	4.87	2.90	0.05	3.06	2.56	1.01
Total	97.6	96.7	97.8	95.2	93.5	94.6	94.5	94.1	99.5	97.2	99.9	98.7	98.4	92.9	96.4	95.8	92.7
Vol%																	
Ol	82.1	59.7	36.7	85.4	47.2	97.7	46.3	62.8	41.6	50.7	25.7	48.6	18.9	78.6	89.9	52.1	78.6
Opx	12.1	10.3	11.5	1.79	7.81	<0.01	28.6	11.3	5.49	4.93	6.75	10.4	0.79	13.8	1.60	3.13	4.74
Cpx	0.57	6.01	5.37	0.99	14.8	0.81	6.47	4.14	3.46	8.82	5.11	7.54	3.27	0.42	0.13	0.36	4.27
Plag	3.19	12.7	13.7	0.74	7.92	0.31	12.4	7.82	5.76	10.5	7.67	15.1	2.6	5.86	3.00	6.63	10.1
Sod	0.02	<0.01	<0.01	0.33	<0.01	0.54	0.02	<0.01	0.01	<0.01	<0.01	0.01	<0.01	0.02	0.32	0.06	0.09
Chr	0.62	0.82	0.77	0.50	0.85	0.29	1.29	0.86	0.64	0.73	1.11	0.71	0.49	1.03	0.33	0.19	0.83
Metal	0.32	2.11	4.56	1.63	1.02	0.30	1.47	4.68	3.59	4.35	6.77	3.32	2.43	0.04	2.03	1.97	0.68
Troi	1.00	8.37	27.5	8.63	20.4	0.04	3.48	8.44	39.4	20.0	46.9	14.4	71.5	0.24	2.72	35.6	0.63

Continued, next page.

Table EA-1-2, continued.

Object	Beg-14 rim	Beg-15	Beg-16A interior	Beg-16A edge	Beg-17	Beg-17 silicate areas	Beg-17A	Beg-18A	NWA-6	NWA-11 core	NWA-11 inner rim	NWA-11A core	NWA-11A rim	NWA-11C rim	NWA-15 core	NWA-21
type	AO-WM, troi-rich	coarse IIAB	AO-U, troi-rich	AO-U, troi-rich	AO-M, troi-rich		matrix lump	fine IIAB	coarse IIAB	coarse IIAB	AO-M	fine IIAB	AO-U, troi-rich	AO-U	coarse IIAB	fine IIAB
N	5	10	5	2	23	10	5	8	10	13	6	13	8	6	13	8
Mg# (at.)	0.69	0.73	0.71	0.87	0.78	0.80	0.67	0.68	0.47	0.73	0.64	0.61	0.67	0.51	0.67	0.64
Wt%																
SiO_2	29.42	40.1	29.4	15.1	32.1	43.5	47.1	36.8	32.9	38.6	36.2	29.3	13.0	25.6	37.4	38.2
Al_2O_3	1.62	2.42	1.59	0.33	2.71	3.73	0.20	1.82	1.50	3.49	2.22	1.17	0.77	1.09	1.89	2.75
Cr_2O_3	0.40	0.54	0.57	0.22	0.56	0.72	0.68	0.62	0.54	0.36	1.83	0.78	0.08	0.34	0.44	0.67
FeO	17.0	16.2	16.3	3.80	13.4	12.02	19.9	22.3	26.5	15.7	23.3	22.1	12.3	31.8	21.8	22.2
MnO	0.30	0.38	0.28	0.13	0.33	0.44	0.82	0.39	0.25	0.42	0.29	0.24	0.12	0.22	0.35	0.32
MgO	21.4	28.0	22.1	13.7	19.5	26.0	22.1	26.9	15.5	22.3	21.3	19.8	8.56	18.8	27.0	24.2
CaO	1.67	2.17	1.96	0.70	1.65	2.22	0.68	2.25	1.70	2.06	3.68	2.56	0.28	0.34	1.01	1.67
Na_2O	0.65	0.27	0.38	0.14	0.31	0.41	0.14	0.24	0.20	0.50	0.39	0.18	0.05	0.08	0.16	0.27
Ni	1.89	0.28	1.44	3.31	0.94	0.47	0.04	0.18	1.87	3.37	0.62	3.57	1.94	1.93	0.49	0.41
S	6.19	0.39	6.97	20.1	8.05	1.77	0.05	0.56	0.23	0.22	0.35	0.42	18.8	0.51	0.07	0.12
Cl	<0.01	<0.01	<0.01	<0.01	0.01	0.01	0.02	0.01	<0.01	0.01	<0.01	0.01	<0.01	<0.01	0.02	<0.01
Fe (troi)	10.8	0.67	12.14	35.1	13.7	3.06	0.09	0.98	0.39	0.38	0.62	0.73	32.7	0.88	0.12	0.21
Fe (met)	4.69	0.71	3.58	8.23	1.17	1.04	0.11	0.45	4.64	5.32	1.54	8.87	4.83	4.79	1.21	1.01
Total	96.1	92.2	96.7	100.8	94.5	95.4	91.9	93.5	86.2	92.7	92.4	89.7	93.4	86.4	91.9	92.0
Vol%																
Ol	64.6	62.2	62.2	31.7	35.7	37.6	9.80	73.6	57.3	53.6	63.8	69.5	36.7	91.6	67.1	59.2
Opx	1.43	22.2	4.07	6.35	29.8	40.8	84.7	9.75	25.5	24.1	10.2	5.50	6.47	<0.01	22.9	25.1
Cpx	6.30	5.31	6.65	3.27	3.31	4.23	3.08	6.36	5.15	3.11	12.3	10.4	0.73	0.07	0.85	1.83
Plag	10.2	8.40	8.38	2.38	8.72	11.8	1.21	8.00	7.09	14.1	9.86	5.05	1.99	3.34	7.35	12.1
Sod	<0.01	0.04	<0.01	<0.01	0.05	0.07	0.23	0.11	0.02	0.13	<0.01	0.07	<0.01	0.01	0.22	0.02
Chr	0.45	0.57	0.65	0.28	0.59	0.73	0.75	0.69	0.67	0.39	2.14	0.89	0.11	0.40	0.48	0.75
Metal	3.23	0.47	2.46	6.32	1.10	0.70	0.07	0.30	3.70	4.20	1.08	7.60	3.94	3.45	0.86	0.70
Troi	13.8	0.86	15.6	49.7	20.7	4.08	0.11	1.19	0.59	0.43	0.78	1.03	50.1	1.17	0.16	0.27

Continued, next page.

Table EA-1-2, concluded.

	Sah98-3 core	Sah98-3 rim	Sah98-3A	Sah98-4B core	Sah98-4B rim	Sah98-5	Sah98-12 core	Sah98-12 rim	Sah98-13 core	Sah98-13 rim
type	fine IIA	AO-U, troi-rich	AO-M	fine IAB-IIAB	fine IIAB	fine IIAB	AO-WM	AO-WM, troi-rich	coarse IIAB	AO-WM, troi-rich
N	8	2	4	4	4	16	8	5	7	9
Mg# (at.)	0.61	0.59	0.73	0.85	0.64	0.69	0.70	0.72	0.74	0.76
Wt%										
SiO_2	33.1	14.8	42.7	46.9	41.1	35.4	37.2	32.1	45.0	31.6
Al_2O_3	2.13	1.89	2.75	4.57	4.62	1.89	1.9	1.68	4.79	1.08
Cr_2O_3	0.61	0.12	0.52	0.70	0.67	0.79	0.7	0.45	0.65	0.56
FeO	26.1	9.72	15.5	8.37	19.5	20.9	19.7	16.7	14.2	16.6
MnO	0.28	0.14	0.25	0.30	0.32	0.35	0.32	0.31	0.31	0.31
MgO	23.0	9.42	20.9	27.9	18.8	26.6	25.6	23.6	21.1	25.2
CaO	0.99	0.43	5.38	4.11	2.55	1.39	3.06	1.55	4.22	1.44
Na_2O	0.26	0.55	0.33	0.57	0.47	0.21	0.36	0.42	0.69	0.25
Ni	0.35	0.81	0.51	0.12	0.16	0.51	0.6	1.3	0.05	0.50
S	0.42	19.3	1.11	0.13	0.25	0.39	0.47	4.84	0.22	5.40
Cl	<0.01	<0.01	0.02	0.01	0.01	<0.01	0.03	<0.01	0.02	0.01
Fe (troi)	0.73	33.5	1.94	0.22	0.43	0.69	0.82	8.44	0.39	9.40
Fe (met)	0.86	2.02	1.26	0.30	0.40	1.26	1.49	3.23	0.13	1.16
Total	88.8	92.7	93.2	94.2	89.4	90.4	92.2	94.6	91.8	93.6
Vol%										
Ol	79.9	37.8	27.8	28.4	30.4	72.8	65.8	62.0	23.2	66.4
Opx	7.20	0	38.1	43.1	45.6	13.3	11.4	<0.01	45.0	9.14
Cpx	0.23	0	18.4	8.65	1.98	2.51	10.7	4.72	9.48	5.00
Plag	10.3	11.4	11.8	18.7	20.4	8.65	9.00	9.20	21.0	5.68
Sod	0.03	0	0.20	0.05	0.06	0.03	0.27	<0.01	0.15	0.05
Chr	0.73	0.15	0.57	0.71	0.75	0.91	0.78	0.52	0.69	0.65
Metal	0.62	1.59	0.83	0.18	0.27	0.88	1.01	2.24	0.08	0.86
Troi	0.98	49.1	2.37	0.25	0.54	0.89	1.03	10.9	0.46	12.2

* Object type: AO-U = AO object, unmelted; AO-WM = AO object, weakly melted; AO-M = AO object, melted; fine II and I = fine Type II and Type I chondrules; coarse II = regular, coarse-grained Type II chondrules. Data corrected for unequal-density-effect. Low wt% totals include effect of analyzing pores and cracks. For the norm, iron was distributed between troilite (FeS), metal alloy (28% Ni, 72% Fe), and the balance distributed in silicates and chromite. N = number of analyses averaged for bulk composition or included in range; Ol = olivine ; Opx = low-Ca pyroxene (enstatite + ferrosilite); Cpx = high-Ca pyroxene (diopside + hedenbergite); Plag plagioclase (anorthite + albite); Sod = sodalite; Chr = chromite (chromite + magnesiochromite); Troi = troilite; Met = FeNi metal alloy. Normative values add to 100% within rounding error.

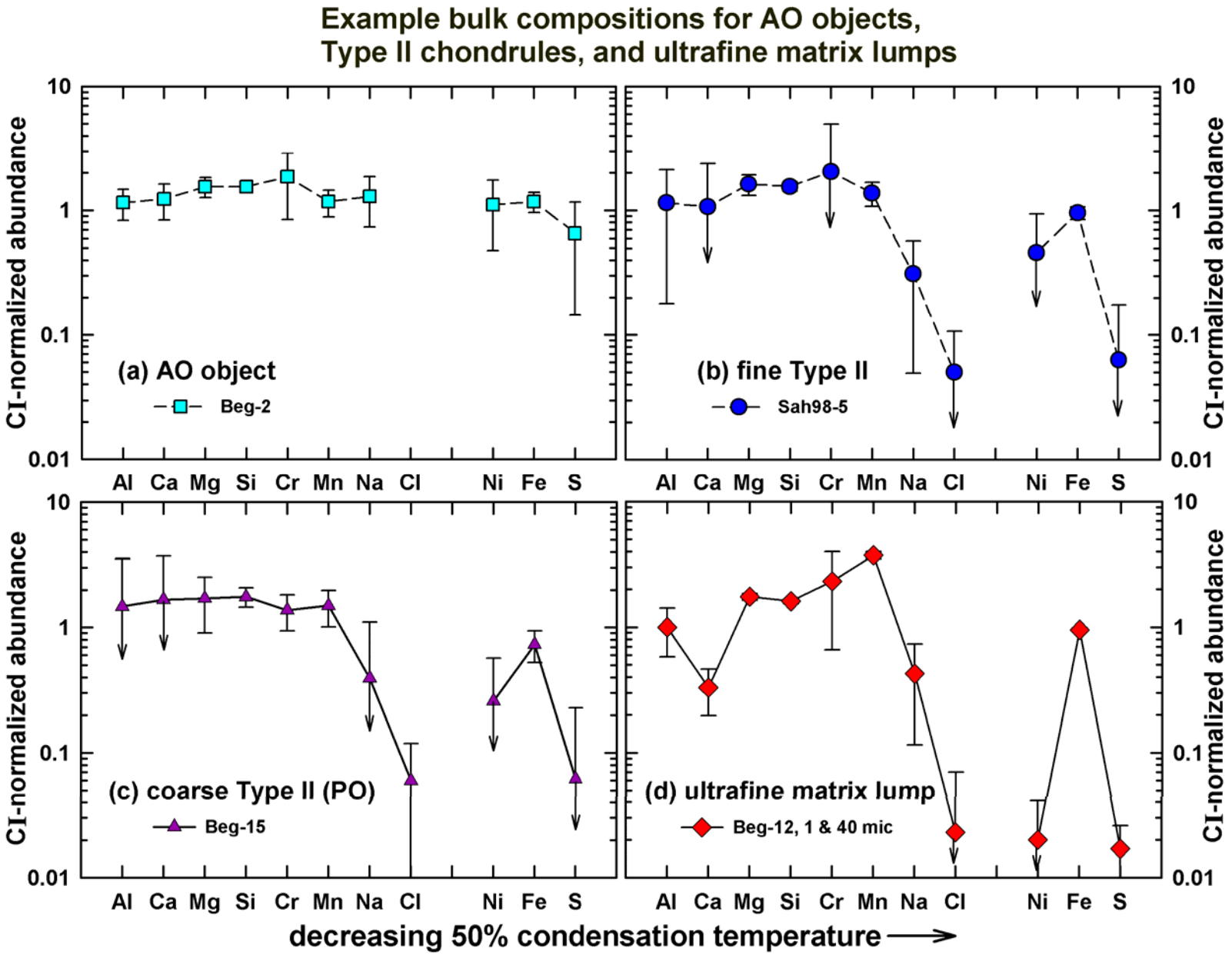

Fig. EA-1-1. Bulk compositions of representative objects determined by DB-EMPA.

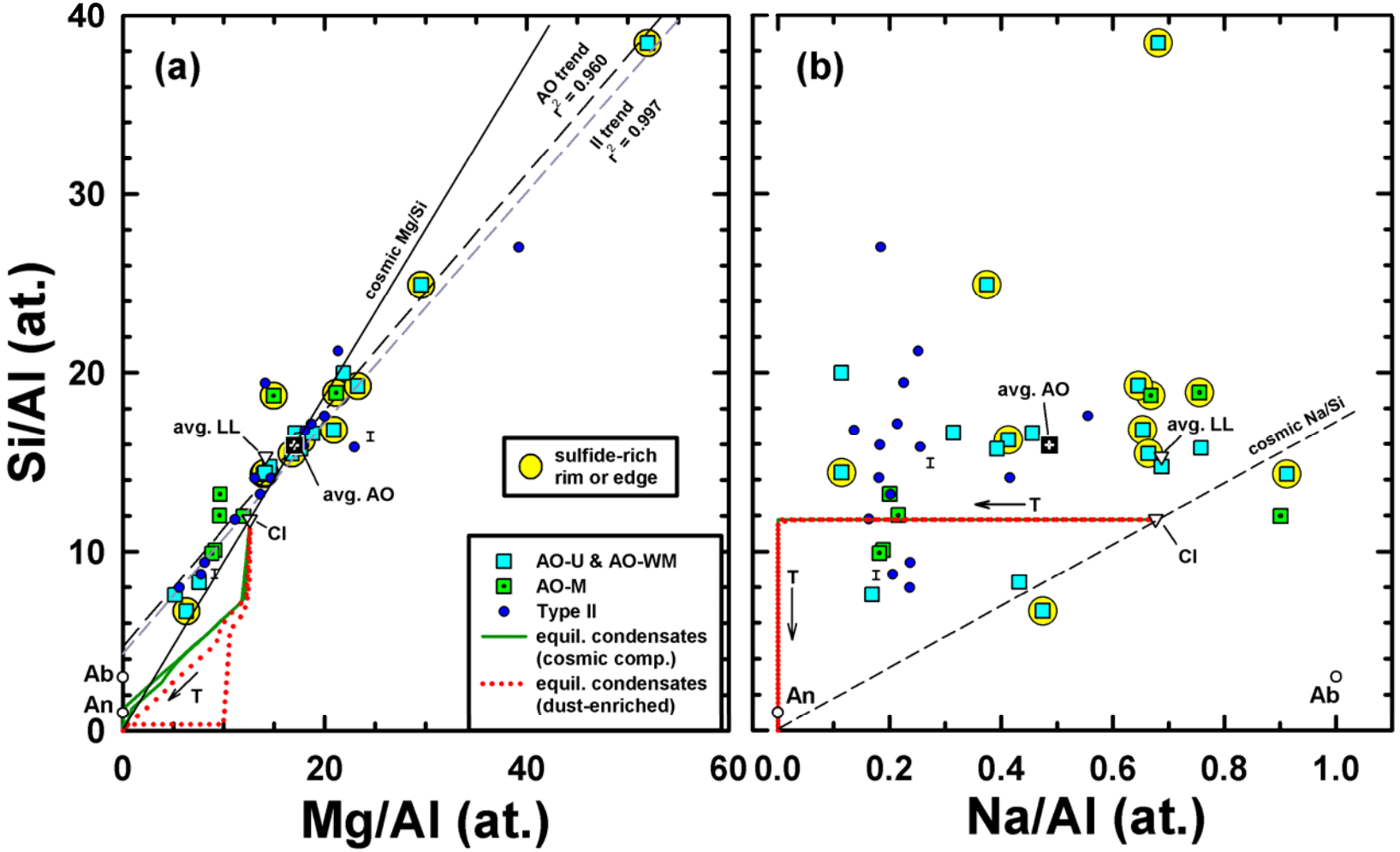

Fig. EA-1-2. Bulk composition of AO and Type II objects compared to equilibrium condensates. CI = average CI chondrite; LL = average LL chondrite, I = objects better described as Type I or transitional Type I-II chondrules. (a) Si/Al vs Mg/Al. (b) Si/Al vs Na/Al.

Electronic Annex EA-2
Trace-element (broad and narrow beam SIMS) data

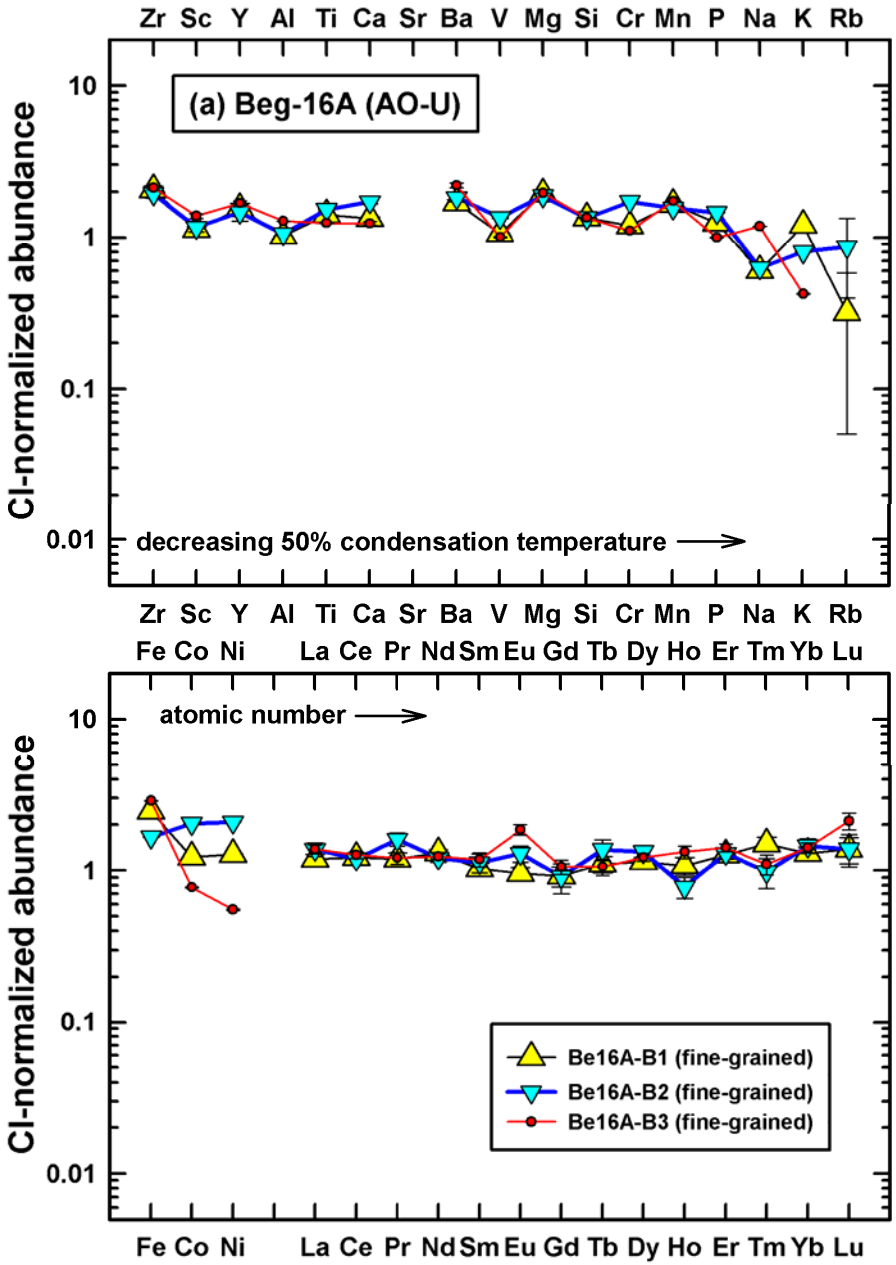

Fig. EA-2a. CI-normalized abundances for SIMS data in Beg-16A, a Type AO-U object. Analyses Be16A-B1, Be16A-B2, and Be16-B3 are broad beam analyses for relatively fine-grained areas in the object. These analyses are examples of the relatively unfractionated pattern type.

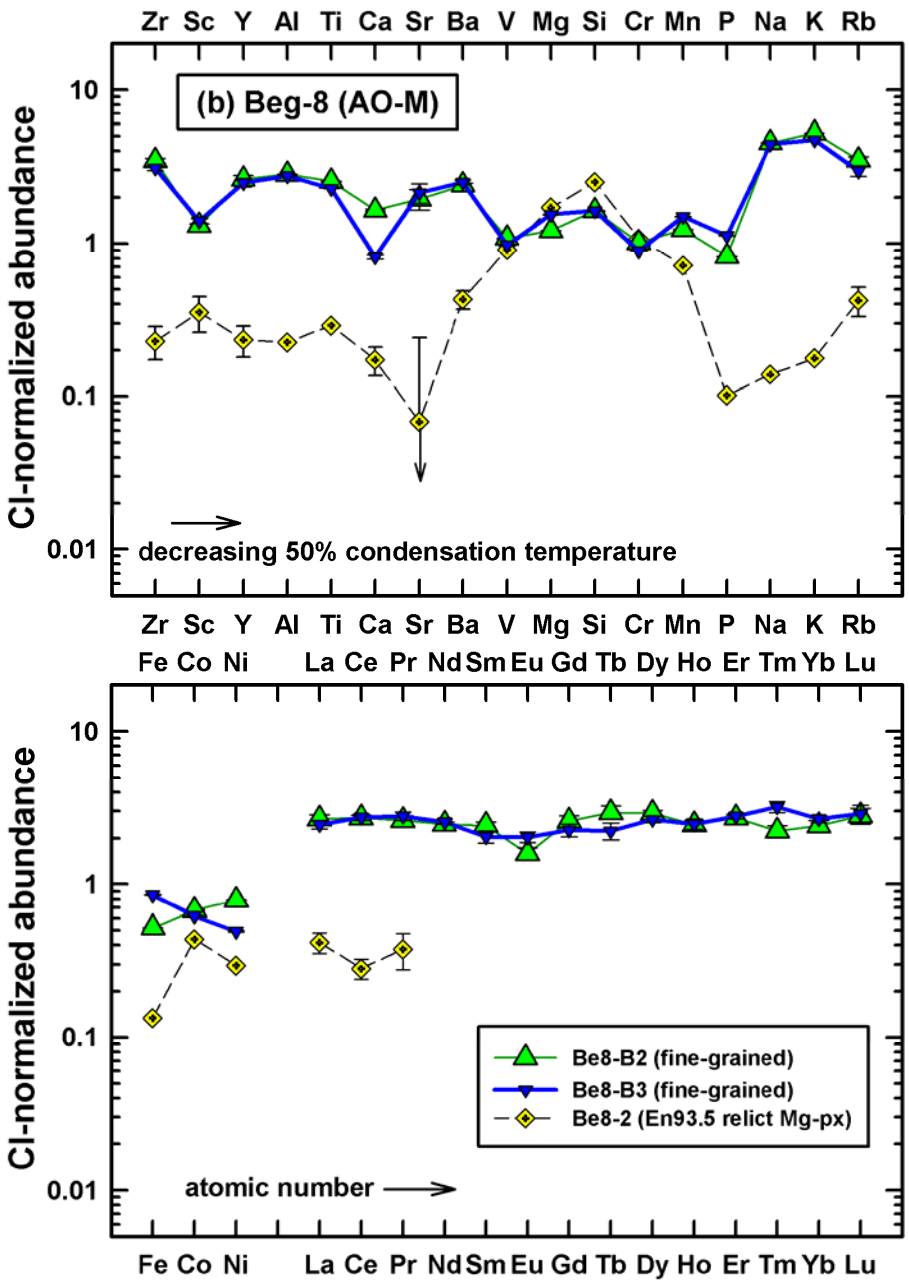

Fig. EA-2b. CI-normalized abundances for SIMS data in Beg-8, a Type AO-M object. Analyses Be8-B2 and Be8-B3 are broad beam analyses for relatively fine-grained areas in the object and are examples of the incompatible-element-enriched pattern type. Analysis Be8-2 is a narrow beam analysis of a relict magnesian low-Ca pyroxene grain.

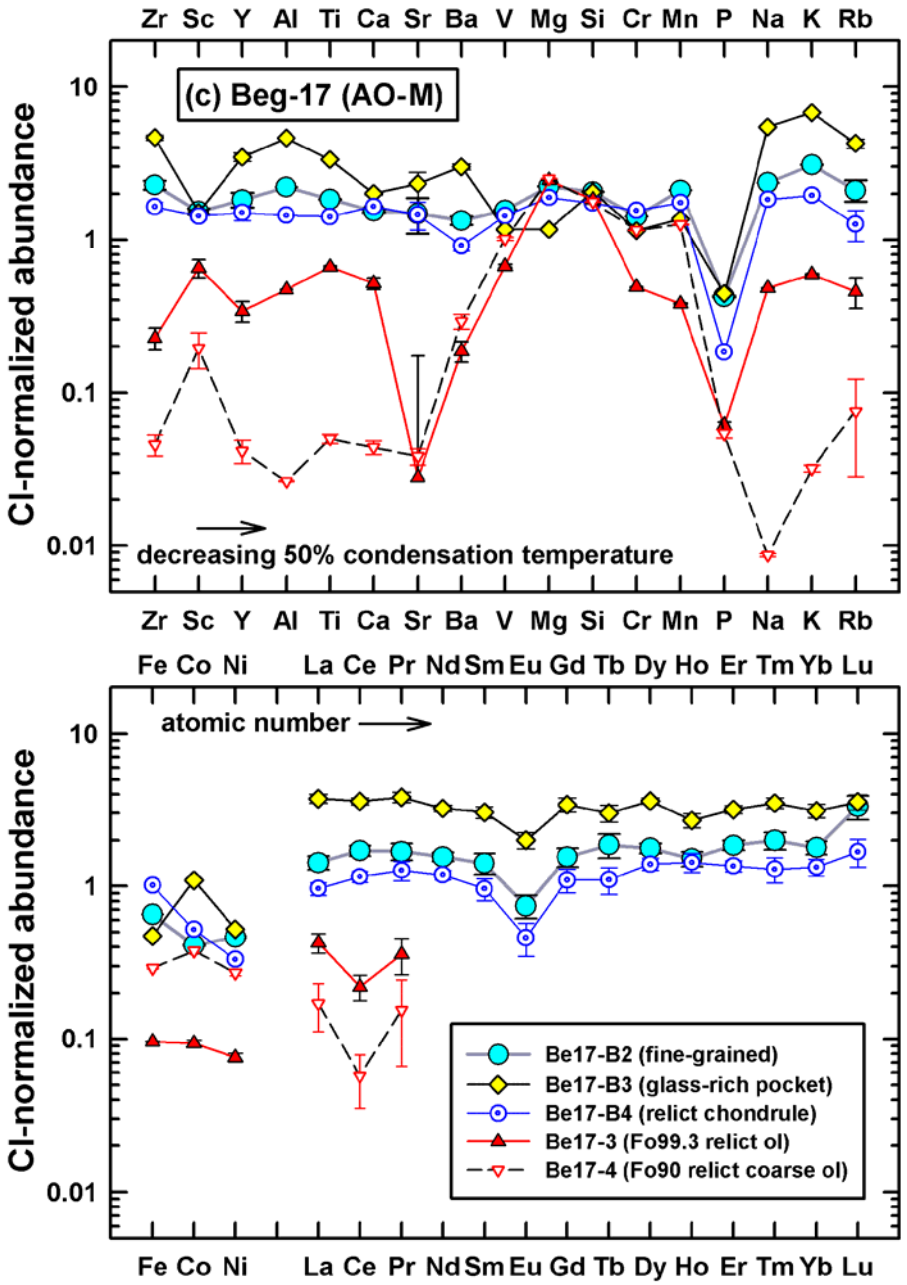

Fig. EA-2c. CI-normalized abundances for SIMS data in object Beg-17, a large Type AO-M object. Analyses Be17-B2 and Be17-B4 are broad beam analyses for a relatively fine-grained area and for a relict chondrule in the object, respectively, with both being examples of the relatively unfractionated pattern type. Analysis Be-B3 is a broad-beam analysis of a glassy area showing an incompatible-element-enriched pattern. All of these analyses are somewhat unusual in showing negative anomalies in P and Eu. Analyses Be17-3 and Be17-4 are narrow beam analyses of two relict olivine grains that have significantly different compositions compared to each other, with the more forsteritic grain being enriched in both refractory lithophile elements and alkali elements.

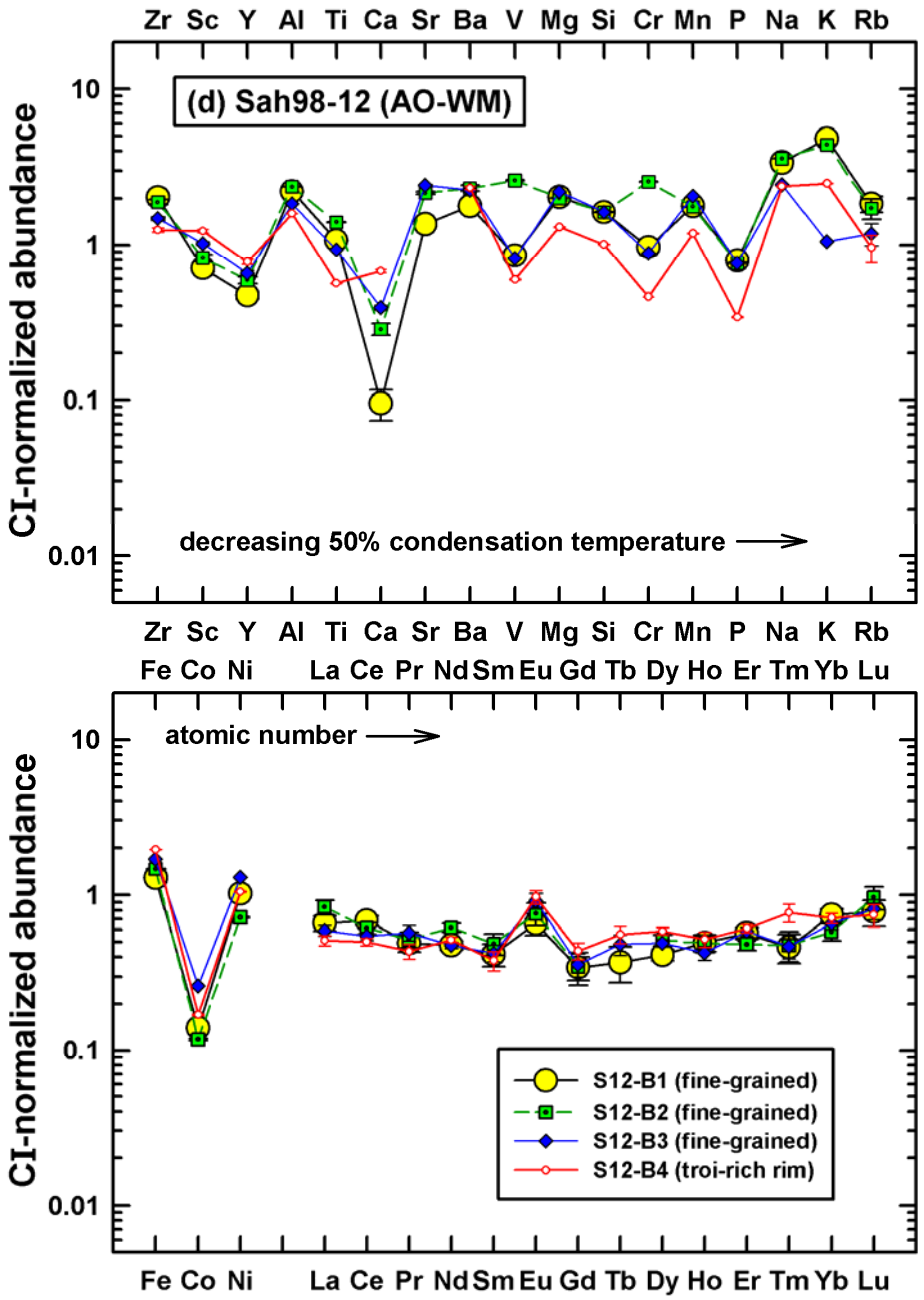

Fig. EA-2d. CI-normalized abundances for SIMS data in object Sah98-12, a Type AO-WM object. Analyses S12-B1, S12-B2, and S12-B3 are broad beam analyses for fine-grained materials and are examples of the fractionated, Ca-REE-poor type pattern, with low abundances of Ca, Co, REE, and Y. Analysis S12-B4 is a broad beam analysis for the troilite-rich outer edge of the object. All analyses show a 'W-shaped' REE pattern characterized by a positive Eu anomaly and otherwise relatively low abundances of the middle REE.

Table EA-2-1. Broad beam SIMS data.

Sahara 99175

object	Sah98-4B	Sah98-4B	Sah98-4B	Sah98-4B	Sah98-5	Sah98-5	Sah98-5	Sah98-12	Sah98-12	Sah98-12	Sah98-12	Sah98-12	Sah98-13	Sah98-13	Sah98-13
position	core	core	rim	rim	interior	interior	interior	interior	interior	interior	edge	rim	rim	rim	rim
object type	fine II	fine II	AO-WM	AO-WM	fine II	fine II	fine II	AO-WM	AO-WM	AO-WM	AO-WM	AO-WM	AO-WM	AO-WM	AO-WM
analyt	54B-B1	54B-B2	54B-B3	54B-B4	55-B2	55-B3	55-B4	512-B1	512-B2	512-B3	512-B4	513-B1	513-B2	513-B3	513-B4
target	ol+px+gl mix, magnesian core	ol+px+gl mix, magnesian core	ol+px+field mix, ferrous rim	ol+px+field mix, ferrous rim	ol+px+field meso	ol+px+field meso	ol+px+field meso	ol+px+field-rich interior	ol+px+field-rich interior	ol+px+field-rich interior	trolilite-rich edge	iron-rich	rim ol+px+field mix	rim ol+px+field mix	rim ol+px+field mix
chemical type	fractionated, Al-rich	fractionated, Al-rich	fractionated, Al-rich	fractionated, Ca-REE poor	unfractionated	unfractionated	fractionated, Ca-REE poor	unfractionated	fractionated, Ca-REE poor	fractionated, Ca-REE poor	unfractionated	unfractionated	fractionated, Ca-REE poor	unfractionated	fractionated, Ca-REE poor
Na mg/g	16.8	23.9	22.8	10.3	9.4	9.02	8.7	16.9	17.9	12.3	12	11.9	13.5	13.7	
Mg wt%	18.1	17.4	20.1	22.3	18.5	19.1	18.4	20.2	19.9	21.9	12.9	17.4	17.5	17.7	
Al wt%	2.14	2.92	2.46	1.66	1.66	1.84	1.74	1.93	2.06	1.61	1.39	1.56	1.59	1.64	
Si wt%	21.9	21.9	19.2	19.2	16.6	16.6	16.6	17.3	17.3	17.3	10.7	14.8	14.8	14.8	
P ug/g	420	175	2840	885	910	1000	1050	965	927	928	415	1110	1200	930	
K mg/g	2.03	2.79	1.58	0.697	1.23	1.6	1.91	2.67	2.45	0.586	1.39	1.79	1.15	1.82	
Ca wt%	1.86	2.32	2.51	0.446	1.57	0.525	1.27	0.088	0.264	0.363	0.628	0.348	0.468	0.419	
Sc ug/g	9.53	9.09	8.71	7.77	8.14	7.31	7.8	4.1	4.79	5.95	7.16	6.07	6.26	6.05	
Ti ug/g	1000	1250	1240	874	665	466	617	468	613	406	246	345	539	418	
V ug/g	90.9	89.8	125	79.5	78.1	48	79.5	48.1	148	46.2	33.6	48.2	64.3	71.2	
Cr mg/g	4.51	4.69	8.09	5.27	3.3	2.28	3.96	2.57	6.81	2.35	1.22	2.43	3.39	3.61	
Mn mg/g	2.77	2.77	5.31	5.5	3.1	3.32	3.34	3.55	3.52	4.11	2.37	2.91	2.97	2.91	
Fe wt%	11	12.6	81.5	56	18.8	25.1	25.2	24.5	27.9	32.5	37.3	19.7	20.8	26.2	
Co mg/g	0.349	0.211	2.48	0.311	0.03	0.0935	0.157	0.0703	0.0591	0.131	0.0856	0.041	0.0965	0.0875	
Ni mg/g	4.64	47	5.75	7.14	7.6	8.21	10.1	7.07	13.1	10.6	5.41	10.8	10.8	10.5	
Rb ug/g	2.74	6.27	7.98	2.82	5.74	3.83	4.37	4.24	3.97	2.72	2.21	4.94	2.72	3.78	
Sr ug/g		6.58	37.8	11.6	3.75	28.8	6.23	21.9	10.6	16.9	19	31.4	12.7	24.5	26
Y ug/g	3.63	5.02	6.4	1.88	2.5	1.41	2.8	0.734	0.921	1.02	1.21	1.11	1.69	1.33	
Zr ug/g	11.6	17.2	19.9	9.69	8.18	8.89	8.73	8.01	7.46	5.87	4.93	6.72	7.55	6.42	
Ba ug/g	0.713	0.658	2.07	3.41	0.955	6.77	6.69	4.17	5.44	5.29	5.47	6.86	5.09	5.54	
La ng/g	601	780	1030	248	313	212	227	155	197	139	120	177	227	196	
Ce ng/g	1560	2170	2830	647	743	516	608	414	370	329	302	416	735	475	
Pr ng/g	213	289	380	66.1	130	79.9	87.2	43.8	46.2	50.9	38.9	57.3	108	61.1	
Nd ng/g	1060	1410	2040	386	581	338	485	215	280	216	233	272	440	306	
Sm ng/g	329	389	549	82.8	214	79.5	206	61.3	71.7	62.5	56	85.2	146	94.2	
Eu ng/g	59.1	68.8	255	46.3	45.5	78.8	85.1	36.8	42.6	51.5	54.5	51.5	66.5	62.3	
Gd ng/g	439	530	803	94.4	282	128	245	67.6	67.9	70.7	86.1	124	212	130	
Tb ng/g	62.9	114	160	21.8	59	33.1	52.9	13.4		17.5	20.2	19.9	49.2	23.8	
Dy ng/g	583	774	947	199	364	191	376	100	125	120	142	169	272	173	
Ho ng/g	117	163	176	61.5	81.3	43.6	80.9	27.5	27.2	23.7	28.9	43.8	61.9	39.1	
Er ng/g	418	528	601	152	293	164	244	90.3	76.9	92.7	97	116	189	132	
Tm ng/g	59.5	73.4	79.7	34.4	34.7	25	45.2	11.1	11.5	11.3	18.7	17	28.9	16.8	
Yb ng/g	405	503	617	234	266	187	270	122	94	107	116	126	166	125	
Lu ng/g	64	74.8	100	40.2	45	37.3	44.5	19	23.4	19.8	18.1	25.6	25.5	21.9	

NWA 3127

object	NWA-11A	NWA-11A	NWA-11A	NWA-11A	NWA-11C	NWA-11C	NWA-11C	NWA-15	NWA-15	NWA-21	NWA-21	NWA-21	NWA-21	NWA-21
position	core	inner rim	inner rim	outer rim	rim	rim	rim	interior	interior	interior	interior	interior	interior	interior
object type	fine II	AO-U	AO-U	AO-U	AO-WM	AO-WM	AO-WM	coarse II	coarse II	fine II	fine II	fine II	fine II	fine II
analyt	N11A-B1	N11A-B2	N11A-B3	N11A-B4	N11C-B1	N11C-B2	N11C-B3	N15-B1	N15-B2	N21-B1	N21-B2	N21-B3	N21-B3	N21-B3
target	ol+field core meso	fine-grained mafic/anor rim	fine-grained mafic/inner rim	link-rich outer rim	fine-grained rim	fine-grained rim	fine-grained rim	ol+px+field meso	ol+px+field meso	ol+field meso	ol+field meso	ol+field meso	fractionated, Al-rich	fractionated, Al-rich
chemical type	unfractionated	unfractionated	unfractionated	unfractionated	unfractionated	unfractionated	unfractionated	unfractionated	unfractionated	fractionated, Al-rich	fractionated, Al-rich	fractionated, Al-rich	fractionated, Al-rich	fractionated, Al-rich
Na mg/g	4.38	2.15	1.2	0.737	0.943	1.09	1.42	6.27	3.88	12.9	6.84	12.9	12.9		
Mg wt%	16.5	16.8	17.7	8.06	16.3	14.6	14.6	13.4	15.9	18.6	20.1	17.6	17.6		
Al wt%	1.32	0.812	1.11	0.418	0.623	0.754	0.987	2.05	1.81	1.84	1.63	1.9	1.9		
Si wt%	13.7	13.7	6.07	12	12	12	12	17.4	17.4	17.8	17.8	17.8	17.8		
P ug/g	1080	1150	1190	363	865	913	842	1270	903	1470	1450	1590	1500		
K mg/g	1.58	0.314	0.339	0.139	0.23	0.376	0.72	0.834	0.356	2.15	1.97	2.21	2.21		
Ca wt%	0.867	0.98	0.738	0.34	0.501	0.738	1.01	1.61	1.44	1.45	1.03	1.49	1.49		
Sc ug/g	8.16	7.93	7.7	4.23	6.61	6.39	6.96	9.43	8.47	9.13	8.32	8.5	8.5		
Ti ug/g	792	695	626	215	657	633	612	965	826	887	763	898	898		
V ug/g	52.8	50.7	63.5	25.2	75.7	59.3	62.6	86.6	77.8	95.2	68.8	84.5	84.5		
Cr mg/g	1.9	2.21	2.64	1.35	4.05	3.48	2.9	2.76	3.45	5.33	3.32	4.66	4.66		
Mn mg/g	2.27	2.36	2.51	1.53	2.6	2.56	2.62	2.81	2.92	3.23	3.45	3.04	3.04		
Fe wt%	33.3	41	44.3	54.7	42.9	48.3	52.5	17.8	18.2	21.1	26.2	21.2	21.2		
Co mg/g	0.578	0.091	0.682	0.091	1.2	4.85	1.79	0.126	0.131	0.184	0.262	0.225	0.225		
Ni mg/g	19	15	21.3	6.5	19.3	18.6	11.4	1.59	2.2	1.05	2.21	1.68	1.68		
Rb ug/g	8.16	1.64	3.24		2.51	3.41	2.55	5.37	2.44	9.44	7.48	9.21	9.21		
Sr ug/g	14.8	11.9	14.9	20.2	11.9	6.74	15.9	19.9	14.8	14.8	18.4	20.8	20.8		
Y ug/g	3.06	2.43	2.77	1.31	2.02	2.16	2.59	2.6	1.8	2.98	2.7	2.93	2.93		
Zr ug/g	10.5	10.3	8.89	4.79	7.28	9.66	10.3	14.5	10.9	9.23	9.08	9.52	9.52		
Ba ug/g	2.82	1.84	1.58	0.669	0.54	0.86	1.05	3.91	3.69	4.33	3.2	3.85	3.85		
La ng/g	377	368	76.8	216	172	220	360	275	477	403	469	469	469		
Ce ng/g	1170	991	965	214	577	557	597	949	658	1020	1080	1140	1140		
Pr ng/g	186	133	113	35.2	76.3	96.9	90.7	142	119	179	163	183	183		
Nd ng/g	867	718	639	185	449	466	445	708	487	832	672	759	759		
Sm ng/g	227	188	170	40.2	146	150	133	208	101	243	259	236	236		
Eu ng/g	43.5	36.4	41.8	11.7	33.4	45.6	44.6	106	67.7	67	85.9	89.1	89.1		
Gd ng/g	304	219	279	73	175	199	237	315	184	307	307	351	351		
Tb ng/g	51.7	43.7	49.9	14.2	40.1	49.4	46	59.9	45.8	71.8	64.3	68.5	68.5		
Dy ng/g	453	316	401	113	294	306	350	424	344	471	473	467	467		
Ho ng/g	91.3	72.6	107	30.4	68.5	55.5	69.2	87.2	68.6	118	91.3	119	119		
Er ng/g	247	257	276	84.5	199	224	223	284	195	345	329	329	329		
Tm ng/g	60.2	39.1	34.4	14	30.6	36.3	33.8	40.2	33.9	52	40.7	45.6	45.6		
Yb ng/g	341	266	284	106	260	251	301	279	199	373	345	316	316		
Lu ng/g	58.1	32.5	50.1	20.3	33.8	39.7	43.3	46.3	42.9	65.2	60.4	46.8	46.8		

NWA 4930

object	Beg-2	Beg-2	Beg-2	Beg-2	Beg-3	Beg-3	Beg-3	Beg-3	Beg-6	Beg-6	Beg-6	Beg-6	Beg-6	Beg-6	Beg-6	Beg-6	Beg-8	Beg-8	Beg-12	Beg-12	Beg-14	Beg-14	Beg-14	Beg-16A	Beg-16A	Beg-16A	Beg-16A	Beg-17	Beg-17	Beg-17	Beg-17A	Beg-17A
position	interior	interior	interior	interior	interior	interior	interior	interior	core	rim	rim	rim	rim	rim	rim	rim	interior	interior	interior	interior	core	core	rim	interior	interior	interior	interior	interior	interior	rim	interior	interior
object type	AO-U	AO-U	AO-U	AO-U	AO-U	AO-U	AO-U	AO-U	fine II	fine II	fine II	fine II	fine II	fine II	fine II	fine II	AO-M	AO-M	matrix	matrix	fine II	fine II	AO-WM	AO-U	AO-U	AO-U	AO-U	AO-U	AO-M	AO-M	matrix	matrix
analyt	Be2-B1	Be2-B2	Be2-B3	Be2-B4	Be3-B1	Be3-B2	Be3-B3	Be3-B4	Be6-B1	Be6-B2	Be6-B3	Be6-B4	Be6-B5	Be6-B6	Be6-B7	Be6-B8	Be8-B2	Be8-B3	Be12-B1	Be12-B2	Be14-B1	Be14-B2	Be14-B3	Be16A-B1	Be16A-B2	Be16A-B3	Be16A-B4	Be17-B2	Be17-B3	Be17-B5	Be17-B4	Be17A-B1	Be17A-B2
target	ol+px+field mix	ol+px+field mix	ol+px+field mix	ol+px cluster	ol+px+field mix	ol+px+field mix	ol+px+field mix	missed CAI, "analyzed grain to NW"	fine-grained core	fine-grained core	fine-grained core	fine-grained core	inner rim	inner rim	outer rim, mix-rich	outer rim, mix-rich	ol+px+field meso	ol+px+field meso	ol+px+field meso	matrix-like lump	fine ol+field+px mix (core)	fine ol+field+px mix (core)	fine ol+field+px mix (core)	fine ol+field+px	fine ol+field+px	fine ol+field+px	fine ol+field+px	fine ol+field+px	glass-rich pocket	relict chondrule, ol + meso overlap	matrix-like lump	matrix-like lump
chemical type	unfractionated	unfractionated	unfractionated	unfractionated	unfractionated	unfractionated	unfractionated	unfractionated	unfractionated	unfractionated	unfractionated	unfractionated	unfractionated	unfractionated	unfractionated	unfractionated	unfractionated	unfractionated	fractionated, Al-rich	fractionated, Al-rich	unfractionated	unfractionated	unfractionated	unfractionated	unfractionated	unfractionated	unfractionated	unfractionated	fractionated, Al-rich	unfractionated	fractionated, Al-rich	fractionated, Al-rich
Na mg/g	10.9	11.1	7.91	6.5	9.14	10.4	11.5	8.15	12.2	7.19	2.64	3.74	4.57	2.88	5.09	20.1	19.7	7.32	8.26	9.96	4.33	7.5	2.88	3	5.67	10.9	25.4	9.15	2.38	1.65		
Mg wt%	20.1	17.6	15.9	15.8	11.3	11.2	11.2	18	16.9	18.1	24.7	14.3	15.1	7.07	12.8	10.7	13.6	22.7	20.6	14.6	21.1	18	18.3	17.7	18.6	20.5	10.7	18.7	15.4	16.2		
Al wt%	1.4	1.31	1.25	0.97	1.46	1.92	1.87	1.39	2.03	1.78	1.53	1.28	1.16	0.51	1.65	2.18	2.14	1.33	1.55	1.93	0.9	1.58	0.846	0.877	1.07	1.78	3.72	1.26	0.3	0.088		
Si wt%	16.3	16.3	16.3	18.3	12.2	12.2	12.2	13.6	18.5	18.5	18.5	13	13	5.32	13	15.4	15.4	17.1	17.1	15.7	15.7	15.7	13.7	13.7	13.7	20.3	20.3	18.4	22	22		
P ug/g	1660	1240	1160	413	1180	1180	1490	996	1010	1070	1150	1490	1470	509	1000	895	1220	577	595	1580	774	1090	1450	1300	1170	478	592	224	213	164		
K mg/g	1.56	1.28	1.27	0.821	0.359	0.574	0.822	0.199	1.81	1.39	0.614	0.745	0.906	0.221	1.31	2.59	2.34	1	1.42	1.82	0.731	1.31	0.642	0.429	0.224	1.8	3.51	1.09	0.348	0.065		
Ca wt%	0.677	1.1	1.57	2.64	1.49	1.04	0.965	1.58	1.47	1.54	0.46	1.12	0.509	0.495	0.915	1.36	0.675	0.275	0.261	2.06	0.678	0.974	1.18	1.52	1.1	1.32	1.73	1.53	0.509	0.629		
Sc ug/g	7.21	5.89	6.77	12.7	5.64	4.86	5.32	7.97	8.33	8.62	7.94	6.13	5.53	3.29	4.92	6.77	7.27	5.87	5.73	8.85	6.42	6.59	6.27	6.47	7.71	8.27	8.15	8.32	2.64	3.41		
Ti ug/g	607	582	615	652	470	557	542	666	890	764	637	533	561	274	485	987	885	528	639	1150	407	737	586	638	520	744	1350	618	267	185		
V ug/g	66.1	59.6	69.3	118	37.5	42.3	37.5	86	68.4	68	89.9	49.7	47.8	28.8	37.2	54.4	48.9	71.3	74.8	68.1	58.1	186	57.4	73.2	54.4	81.7	61	80.9	54.7	47.1		
Cr mg/g	3.96	2.97	3.45	5.21	1.58	2.02	1.58	5.32	3.05	2.94	4.93	2.22	2.08	1.04	1.38	2.4	2.12	4.91	3.88	2.78	2.61	10.64	3.05	4.38	2.82	3.5	2.82	4.12	6.61	5.48		
Mn mg/g	3.27	3.05	2.67	3.28	2.16	2.11	2.2	3.34	3.17	3.29	4.68	2.71	2.76	1.26	2.55	2.18	2.65	9.32	8.35	2.76	3.2	2.86	3.16	2.97	3.31	3.89	2.52	3.47	7.59	7.96		
Fe wt%	26.8	17.9	19.7	19.6	22.3	19.8	21.7	80.2	15.9	20	39.6	29.3	22.5	63.1	25.7	8.79	14.5	24.8	22.7	22.7	21.2	18.2	44.9	30.3	52.5	11.6	8.36	19.3	20.2	19.1		
Co mg/g	0.589	0.265	0.418	0.419	0.498	0.223	0.339	3.61	0.143	0.348	5.61	0.905	0.956	0.941	0.191	0.302	0.277	0.0351	0.0365	0.854	0.24	0.217	0.589	0.981	0.371	0.191	0.508	0.262	0.0552	0.031		
Ni mg/g	15.4	6.62	11.5	11.1	6.78	3.4	6.23	30.6	1.77	5.21	55.9	17.2	9.33	16.7	3.69	7.08	4.44	0.121	0.172	14.6	3.04	3.17	12.4	20.1	5.34	4.35	4.9	3.35	0.67	0.096		
Rb ug/g	6.48	5.45	7.39	3.67	1.39	2.42	3.19		6.16	5.03	7.78	3.22	3.98		3.53	7.14	6.09	4.17	6.58	5.59	2.63	3.67	0.697	1.91				2.9	2.51	0.971		
Sr ug/g	11	11.8	15.5	11.3	24	24	17.7	50	4.88	8.63	22.1	14.2	12	36.3		13.5	14.8	1.63	3.6	22.9	7.19	10.1	27.1	30.6	41.1	10.7	16.8	11.4	6.21	6.04		
Y ug/g	1.92	2.03	2.53	2.8	2.77	2.04	2.94	3.01	3.02	2.79	2.18	2.58	1.94	1.78	1.2	3.64	3.45	2.03	1.71	4.9	1.34	2.14	2.31	2.18	2.52	2.64	5.03	2.34	1.32	0.681		
Zr ug/g	7.86	6.97	7.04	5.57	9.93	8.83	9.57	9.9	9.86	8.86	9.05	6.76	7.21	5.96	5.35	12.2	10.9	6.6	5.78	12.6	4.35	7.2	7.75	7.31	7.99	8.34	17	6.48	3.96	1.39		
Ba ug/g	3.01	2.33	2.02	3.22	4.31	3.71	3.83	4.56	3.93	3.32	3.62	3.56	3.76	2.43	2.46	4.99	5.21	3.72	3.08	4.42	2.83	3.64	3.8	4.08	4.92	2.88	6.52	2.13	0.51	0.404		
La ng/g	250	295	339	186	285	235	357	143	511	336	327	364	383	160	292	558	512	282	258	680	184	335	267	311	311	310	815	226	316	65.2		
Ce ng/g	737	709	948	635	749	632	881	472	1230	1010	814	973	841	348	575	1450	1470	830	685	1770	558	749	708	688	732	957	2020	697	845	187		
Pr ng/g	107	112	123	87.8	115	83.5	126	52.3	153	156	135	148	134	52.1	118	208	221	109	84.6	292	86	128	102	137	103	139	316	113	135	28.5		
Nd ng/g	453	501	638	516	502	413	659	456	889	738	539	622	635	308	514	991	1030	521	473	1368	346	579	569	524	535	653	1360	537	612	106		
Sm ng/g	126	178	185	191	178	130	221	99.3	246	197	176	200	157	80.3	158	317	288	184	139	404	124	162	144	159	167	193	415	142	169	40.6		
Eu ng/g	26	29.7	74.4	50	59.5	71	60.2	79.7	60.7	41.7	88.7	75.9	48.7	40.9	65.3	79.2	101	56.8	54.1	116	32.4	49.9	51.3	69.5	99.7	38.5	104	25.8	51.1	17.4		
Gd ng/g	136	176	141	270	291	179	259	171	380	213	184	265	252	95.6	105	453	395	196	166	464	162	235	173	171	199	283	623	216	191	67		
Tb ng/g	35.4	36.5	38.1	56	37.8	42.9	41.2	48.1	77.4	50.6	44.9	53.1	33.9	21.7	39.2	95.1	72	45.7	36.8	84.9	34.4	30.6	38.3	47.9	36.8	62.6	101	40.1	28.4	16		
Dy ng/g	253	313	435	420	326	304	387	355	515	441	287	379	312	153	273	627	573	309	276	701	211	339	266	310	285	398	815	338	229	102		
Ho ng/g	64.5	76.2	76	106	65.5	52.3	86.1	64.3	120	101	39.1	96.4	64.4	35	53.1	121	123	62.5	69.5	167	43.5	68.2	57	41.2	70.7	78	139	79.5	36.6	25.8		
Er ng/g	161	185	271	261	244	236	281	215	353	287	234	234	190	114	166	385	394	228	178	486	150	239	193	197	216	273	467	215	137	73.3		
Tm ng/g	28	21.6	30.5	40	40.5	32	41	28.5	42.3	40.8	43.7	37.3	31.2	14.2	18.2	47.9	68.8	24.8	18.1	79.9	29.4	34.7	22.8	25.5	44.7	78.4		31.3	15	10.8		
Yb ng/g	191	209	220	249	268	230	241	258	323	303	224	268	217	120	195	349	387	247	171	480	166	245	203	227	221	270	469	216	103	81.1		
Lu ng/g	28	28.3	52.2	47	45.7	36.3	47.5	33.8	62.5	55.7	40.7	42.7	38.7	19.4	36.1	60.7	62.5	45.5	30.1	83.1	31.9	37.8	32.2	32.3	49.3	74.6	80.2	40.7	24.6	19.8		